JOURNAL OF SPACECRAFT AND ROCKETS
Vol. 45, No. 3, May–June 2008

Active Vibration Control of a Deployable Optical Telescope

Steven A. Lane* and Seth L. Lacy†
U.S. Air Force Research Laboratory,
Kirtland Air Force Base, New Mexico 87117
Vit Babuska‡
Sandia National Laboratory, Albuquerque, New Mexico 87185
Stephen Hanes§
The Boeing Company, Albuquerque, New Mexico 87185
and
Karl Schrader¶ and Robert Fuentes¶
Boeing–SVS, Inc., Albuquerque, New Mexico 87109

DOI: 10.2514/1.30838

The U.S. Air Force Research Laboratory developed the deployable optical telescope testbed as part of the large deployable optics research program. The goal of this program was to investigate the feasibility of a deployable space telescope concept and to mature critical enabling technologies to provide risk reduction for the general mission concept. This paper discusses many of the challenges encountered in laboratory testing of complex, sensitive, deployable systems. Implementation of a white-light interferometer for initialization and calibration, a pencil beam or single-pixel heterodyne interferometer for measuring primary mirror motion, and a Twyman–Green interferometer system for wave-front monitoring are discussed. Development of integrated system models and system identification methods for controller design are discussed. Active structural control was demonstrated to maintain optical alignment of the telescope while subjected to simulated reaction wheel disturbances, ambient vibration and atmospheric beam steering. Wave-front sensing and interferogram analysis were used to quantitatively assess optical performance, but wave-front error was not fed back to the controller.

I. Introduction

THE ability of a telescope to resolve distant objects is largely dependent upon the size of its aperture. As a design point, consider that the primary mirror of the Hubble Space Telescope is approximately 2.4 m in diameter, consisting of a single glass monolith (828 kg).** The largest-diameter launch vehicles currently available are approximately 5 m (the evolved expendable launch vehicle, Arianne V, and the space shuttle), which imposes limits on the maximum diameter of a monolithic system. The maximum mass would be a function of the overall payload mass and the desired orbital altitude. Consequently, to put a significantly larger aperture than Hubble into orbit would require an optical platform with a segmented primary mirror and with lower area density. The James Webb Space Telescope (JWST) will use 18 mirror segments that are stacked for launch and then deployed in space to form a 6.5-m-diam primary mirror.†† Mirror segments are being constructed from beryllium to yield a mirror that is exceptionally lightweight while maintaining the necessary structural integrity. The mass of the primary mirror for JWST is estimated to be 705 kg.

A key technical challenge for deployable space telescopes is that mirror segments must be precisely aligned relative to each other, and the optical pathways must be maintained to nanometer tolerances to achieve the necessary optical wave-front coherence and image quality. Lightweight composite structures tend to exhibit lightly damped resonances that cause large-amplitude motion when excited. Low-frequency motion (less than 1 Hz) can induce pointing error and defocus. Such motion may be caused by gravity gradients, solar pressure, or thermal gradients. Higher-frequency motion (1–100 Hz) can cause line-of-sight jitter. Such motion may be induced by microlurch in hinges or latches, popping or drying effects of composite materials, or excitation of structural modes by the spacecraft's attitude control system [1]. Vibration at even higher frequencies poses the risk of coupling with optical elements, causing high-order wave-front distortions. Developing a large deployable optical system will therefore require advances in many technical areas, including 1) integrated system modeling and validation, 2) active vibration control design and implementation, 3) on-orbit system identification, 4) structural and optical metrology, and 5) wave-front sensing and control.

II. Background and Overview

A. Background

There has been significant research since the 1970s to overcome scientific and engineering challenges to enable deployable optical systems. The Strategic Defense Initiative motivated research for deployment and control of beam expanders. Early research was typically performed at the component level, and only in the mid 1990s did system-level hardware testing receive significant attention. Prior work is well documented in the open literature, but a few pertinent examples will be given here.

A series of research efforts conducted by Litton Itek Optical Systems in the 1980s investigated the application of adaptive optics on large apertures. This led to the Large-Aperture Mirror Program (LAMP) testbed, which consisted of a 4-m-diam, segmented, active

Received 5 March 2007; revision received 17 July 2007; accepted for publication 4 August 2007.

*Senior Aerospace Engineer, Space Vehicles Directorate, 3550 Aberdeen Avenue. Senior Member AIAA.
†Research Aerospace Engineer, Space Vehicles Directorate, 3550 Aberdeen Avenue.
‡Senior Research Scientist, Department 1525, Building 880. Senior Member AIAA.
§Senior Optical Physicist, P.O. Box 5670.
¶Senior Control Engineer, 4411 The 25 Way Northeast, Suite 350.

**Data available online at http://hubblesite.org/ [retrieved 15 February 2008].
††Data available online at http://www.jwst.nasa.gov/ [retrieved 15 February 2008].

(deformable) mirror that was developed as a beam expander [2]. Subsequent to LAMP, the adaptive large optics technology (ALOT) research program concentrated on imaging systems and applications [3]. The ALOT program began in 1987 and ended in 1994. The program demonstrated continuous monitoring and correction of image quality without imposing additional constraints on the system's image acquisition. ALOT demonstrated technologies for segmented mirror alignment, real-time figure control, and low-frequency wave-front sensing and control.

In the early 1990s, work was done by Carrier and Aubrun [4] on the Advanced Structures and Controls Integrated Experiment (ASCIE) at the Lockheed Martin Advanced Technology Center. The ASCIE testbed was a full-scale testbed designed to simulate the structural behavior of a telescope with a segmented primary mirror. Much of that work concentrated on developing numerically tractable and robust methods to model and structurally control large, complex, flexible systems. One objective of their research was to evaluate how accurately the dynamic behavior of such a structure could be predicted with finite element analysis. A second objective was to develop structural control methods to improve segment alignment and achieve wideband structural vibration suppression. Because classical modal testing of large systems is costly and difficult, Carrier and Aubrun [4] used frequency-response functions measured with active control sensors and actuators to obtain modeling data for ASCIE. They asserted that this was more representative of on-orbit testing of space structures. They successfully demonstrated methods to model system dynamics online, analytically determine modal characteristics offline, and synthesize system models for controller development from frequency-response measurements up to about 50 Hz.

NASA has been at the forefront of space telescope research and development through their own research centers (such as the NASA Goddard Space Flight Center, the NASA Marshall Space Flight Center, and the NASA Langley Research Center) and through contractors. The Phased-Array-Mirror Extendible Large-Aperture telescope project was initiated in 1989 as a laboratory demonstration of a tactical high-energy laser beam director [5–7]. The NASA Marshall Space Flight Center acquired the testbed in 1993 and used the 36-segment (~7-cm-diam), 0.5-m-aperture telescope to demonstrate wave-front sensing and control. In this system, voice-coil actuators, a Shack–Hartmann wave-front sensor, and inductive edge sensors were used to provide stable control of the segmented primary mirror. Control was demonstrated to about $\lambda/10$ root-mean-square (rms) error (at $\lambda = 633$ nm). Recent work by NASA has focused on facilitating JWST, which uses adaptive optics, wave-front sensing, and lightweight structures [8–11]. NASA Langley Research Center is involved in developing lightweight reflectors, including gossamer structures (about 1 kg/m^2). NASA is also involved in developing ultralightweight, thermally stable, rigid structures for precision deployment, which are capable of high compaction ratios. NASA has supported many university studies, such as research of microdynamic events in precision composite structures [12].

Also during the early 1990s, the Jet Propulsion Laboratory of the California Institute of Technology developed several integrated modeling tools for analysis of large complex optical and interferometric systems. The Integrated Modeling of Optical Systems software package combined structural modeling, optical modeling, and control system design within a common software package executed from MATLAB [13]. The tools were validated on the Micro-Precision Interferometer testbed, a ground-based, full-scale hardware model of a space-based interferometer [14].

During 2001–2002, the Massachusetts Institute of Technology developed a sparse-aperture interferometer testbed called the Adaptive Reconnaissance Golay-3 Optical Satellite (ARGOS) [15,16]. One of the objectives of ARGOS was to demonstrate the feasibility of a modular architecture for space-based optical systems. This testbed was claimed to be the first sparse-aperture array simulating a space-based observatory in a 1-*g* environment, including real-world problems such as coupling between spacecraft structural vibration and wave-front error.

B. UltraLITE

The U.S. Air Force Research Laboratory (AFRL), Space Vehicles Directorate, has been involved in investigating engineering challenges and demonstrating innovative solutions for deployable optical systems to support tactical imaging as well as space-based laser concepts. The AFRL established the Ultra-Lightweight Imaging Technologies Experiment (UltraLITE) program in 1995 to develop and demonstrate a variety of enabling technologies with the goal of the first deployable space telescope flight experiment. The UltraLITE program encompassed several Small Business Innovative Research programs, AFRL technology demonstrations, conceptual design studies, and an integrated ground experiment. Much of this program is documented in various papers [17–19].

Two full-scale technology demonstrations were accomplished under the UltraLITE program related to space-based laser beam expanders. The Space Interactive Control Experiment investigated line-of-sight control and vibration isolation from simulated disturbances such as slewing maneuvers and firing of a chemical laser. The Advanced Structural Experiment was a full-scale beam expander mounted on an air bearing and used to demonstrate technologies such as active structural damping, suppression of slew-induced vibrations, and neural network-type control approaches.

Later technology demonstrations such as the Precision Deployable Optical Structure and the Integrated Hinge Optical Support Structure programs demonstrated deployable structure and hinge concepts traceable to a single petal of a 10-m deployable aperture. These programs investigated deployment repeatability, stability over time, and microdynamic events. Additional smaller efforts concentrated on control algorithm development, precision mechanisms (hinges, latches, and actuators), composite structures, and lightweight mirror technologies. Several component-level flight experiments were accomplished as part of the UltraLITE program, including active vibration control and isolation experiments [20,21].

C. DOT Experiment

The final project completed under the UltraLITE program (subsequently renamed the Large Deployable Optics program in 2001) was an integrated ground experiment referred to as the deployable optical telescope (DOT). The DOT experiment was based on a government-defined space-deployable telescope system concept, which was closely tied to the AFRL flight experiment concept (shown in Fig. 1). The primary objective of the DOT project was to support the development of large-aperture deployable telescopes by demonstrating the feasibility and capability of emerging technologies in an integrated space-traceable testbed. Emerging technologies included lightweight high-stiffness structures (including mirrors), precision deployment mechanisms, system identification (modeling), and structural vibration control. Specific experiment goals included precision deployment and calibration of a segmented telescope and active structural control to maintain calibration while subject to representative spacecraft disturbances. Thresholds established at the beginning of the program for successful control demonstration were as follows:

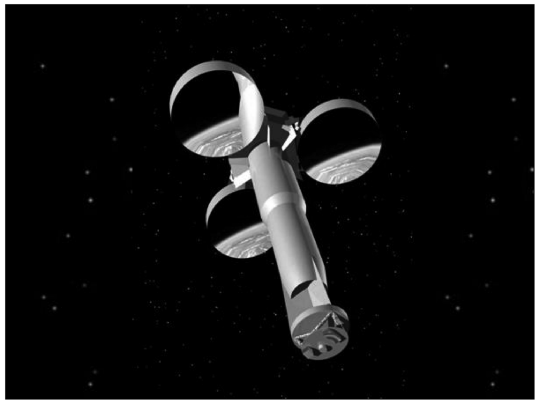

Fig. 1 Illustration of AFRL DOT flight experiment concept.

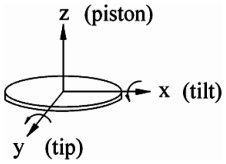

Fig. 2 Definition of mirror segment motion and axes.

1) The primary mirror segment error was not to exceed ± 14 nm (rms over 1000 Hz) in piston motion.

2) The primary mirror error was not to exceed ± 95 nrad (rms over 1000 Hz) in tip and tilt rotation.

Piston motion denotes rigid-body translation, and tip and tilt denote rigid-body rotation, as indicated in Fig. 2.

This testbed provided an unprecedented risk-reduction opportunity for deployable space systems through ground testing and demonstration. It was anticipated that the DOT flight experiment would leverage other technical investments by other programs, government agencies, and industry in areas such as deformable mirrors, adaptive optics, wave-front sensing and control, bus systems, and space-qualifiable electronics. Wave-front sensing was used on DOT only to provide a measure of closed-loop performance (image quality). The measured wave-front error was not fed back to the controller during this phase of the research effort, because the primary goal was active structural control of the integrated system. Nevertheless, the realism and traceability of DOT to a real space telescope distinguishes this experiment from all prior work.

D. Paper Overview

This paper describes the capture, calibration, and maintenance tasks necessary for a deployable optical system. Details of how this was accomplished on the DOT ground demonstration are given: specifically, calibration using white-light interferometry; modeling, system identification, and controller design and implementation using measurements provided by a heterodyne interferometer; and wave-front sensing and analysis using a Twyman–Green interferometer. This is followed by a description of the testbed hardware, experimental setup, and laboratory/test environment. Next, results from tests on DOT are presented that show model fidelity, closed-loop damping, and disturbance rejection. Finally, conclusions and important lessons learned are presented, which we hope will benefit and guide future research efforts.

III. Theory

A. Overview

For a large deployable optical system, precision deployment of the structure once in orbit is the first critical task following initial checkout. The ability of the telescope to constructively combine reflected light from multiple apertures onto a single focal plane requires that deployment actuators, hinges, and latches operate to within millimeter-to-micrometer levels of precision. The initial deployment and coarse-alignment procedure is referred to as the capture phase. In this phase, the orientation of the deployed segments are adjusted such that the optical paths from the primary mirror segments to the secondary mirror and through the aft optics to the focal plane overlap to form a single image (see Fig. 3).

The next step is referred to as calibration. In the calibration phase, actuators on various reflective surfaces are used to fine-tune the optical path lengths to zero-out any optical path length difference between the deployed segments and the focal plane. This step requires measuring and actuating mirror positions at the subwavelength level of precision (approximately 9 nm) and measuring the level of coherence of the recombined wave fronts. In practice, a distant star would provide a broadband point source with collimated wave fronts for calibration.

Once the optical path differences have been minimized, the telescope is considered calibrated, and this becomes the desired operating point, or setpoint, for the telescope. The problem now becomes one of maintaining this setpoint subject to varying thermal loads, pointing/slewing maneuvers, onboard dynamic excitations, and time-varying optomechanical dynamics. Recalibration cycles reduce mission availability. Unlike deep space telescopes, such as Hubble and James Webb, a time-critical tactical mission may preclude allowing a long period of time for disturbances to dissipate on their own. This necessitates the use of on-orbit system identification, active vibration isolation, and active vibration control (i.e., active damping and disturbance rejection). A two-port representation of the control problem is given in Fig. 4. Integrating a structural metrology system to measure the motion of each aperture becomes challenging, especially for a large, lightweight, stiff structure that has little inherent damping. Even small disturbances can saturate sensors and actuators, and so dynamic range becomes a critical issue. The necessary bandwidth of the controller is largely determined by the on-orbit response and optomechanical coupling of the spacecraft. Work by Lake et al. [22] further elaborates on the need to balance passive structural stability and active control requirements for large optic systems. So, in summary, three key steps for deployable telescope operation include 1) capture, 2) calibration, and 3) maintenance.

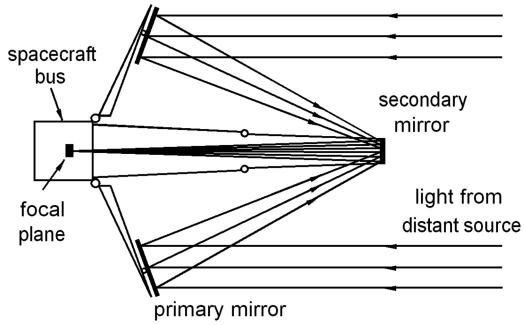

Fig. 3 Illustration of light rays through a deployable telescope.

B. Calibration Using White-light Interferometry

This section focuses on step 2, telescope calibration, which is required for an on-orbit system and for our laboratory system. For the DOT testbed, capture was accomplished through a coarse-alignment procedure in which the light from each subaperture was centered on the focal plane of the telescope. Calibration was accomplished by imaging a point source provided by a white-light interferometer. It is commonly known in optics that imaging a point source yields the point spread function of the optical system (neglecting near-field effects). The point spread function characterizes the optical system in the same manner that an impulse response characterizes a mechanical system.

The optical path length is the effective distance that light waves from the point source travel to the focal plane (relative to traversing the same distance in a vacuum). It is the product of the index of refraction of the media through which the light travels and the physical distance traversed. If the optical path lengths from the point source to each mirror segment and then to the focal plane are all equivalent, then the wave fronts arrive in phase with each other and constructively interfere, which results in the maximum intensity at

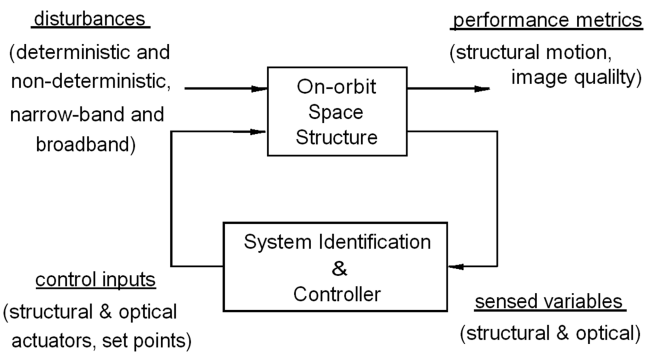

Fig. 4 Two-port representation of the telescope control problem.

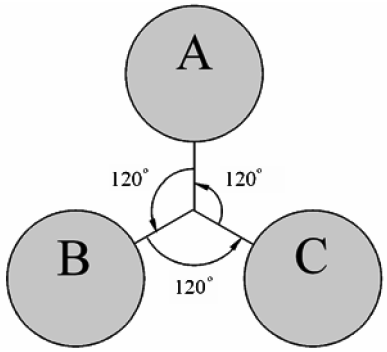

Fig. 5 Depiction of primary mirror segments.

the focal plane. However, if one mirror segment is closer to or further away from the other segments, then there is a nonzero difference in the optical paths, which is referred to as an optical path difference (OPD). Nonzero OPD introduces a phase error that reduces the degree of constructive interference of the combined wave fronts and consequently reduces the intensity measured on the focal plane. This is very similar to the two-slit Young's experiment, except that the source is broadband with an effective mean wavelength of about 500 nm and an effective coherence length of about 900 nm [23].

Consider the primary mirror configuration depicted in Fig. 5 with mirror segments denoted alphabetically. If the OPD is less than the coherence length, the resulting interference (fringe) pattern on the focal plane from any two mirror pairs will be similar to that shown in Fig. 6 (assume that the third mirror has simply been blocked). The light bands indicate constructive interference, and the dark bands indicate destructive interference. The intensity across the focal plane follows a cosine-squared distribution and is modulated by a Bessel function (diffraction term) [23]. If the OPD is greater than the coherence length, then no fringes will be observed, only circles of light resulting from the incoherent combination of the mirror reflections of the point source on the focal plane.

Figure 7 presents the expected interference pattern for the case of all three subapertures perfectly phased. The number of fringes observed is dependent upon several factors, such as source intensity, size of the focal plane, and the size and separation of the subapertures. It is important to note that the fringe pattern from three apertures shown in Fig. 7 is simply the product of the fringe patterns shown in Fig. 6. The intensity distribution across the focal plane is the product of the cosine-squared functions and the square of a first-order Bessel function of the first kind (due to using circular subapertures) divided by its argument, which can be stated as

$$I(r,\theta) \approx \left[\frac{J_1(\beta)}{\beta}\right]^2 \sum_{i=1}^{3} \cos^2(\alpha_i) \tag{1}$$

The definitions of the (unitless) arguments α_i and β are not necessary for a qualitative understanding, and r and θ are coordinates for the focal plane. Suffice it to say that the arguments are functions of wavelength, orientation, and geometry [23]. Figure 8 presents a plot of $(J_1(\beta)/\beta)^2$ and the product of $(J_1(\beta)/\beta)^2\cos^2(\alpha)$, where α is an arbitrary multiple of β. The first zeros of $(J_1(\beta)/\beta)^2$ occur at about ± 3.83. The region of high intensity bounded by the first zeros is referred to as the Airy disk (in two dimensions). Figure 8 shows that

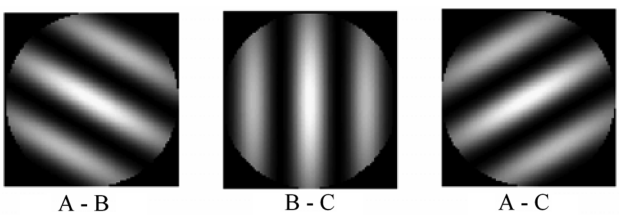

Fig. 6 Depiction of fringe patterns from any two subapertures.

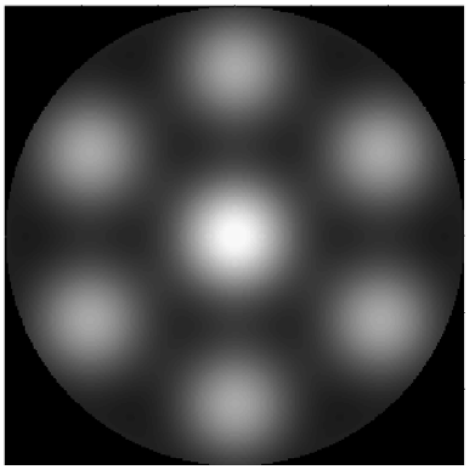

Fig. 7 Illustration of the expected fringe pattern for three subapertures.

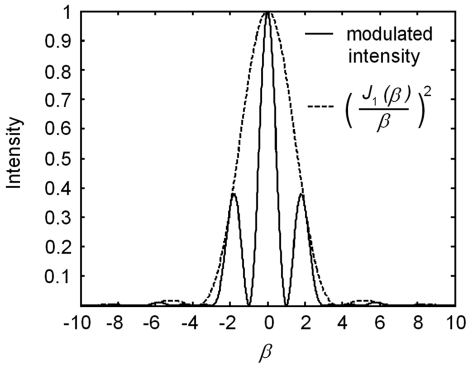

Fig. 8 Plot illustrating the modulated intensity pattern on the focal plane.

the diffraction term modulates the intensity of the interference fringes. For the example case shown in Fig. 8, there are three fringes within the region of the Airy disk, which is the same as that depicted in Fig. 7.

With zero OPD, the contrast between the destructive interference regions and the constructive interference regions is maximized. As the OPD increases, fringes start shifting, resulting in less than maximum intensity at the central peak and resulting in less contrast between the light and dark regions. To illustrate, Fig. 9 presents an actual image taken from DOT during the calibration procedure. The Airy disk is circled in white. One can observe additional side lobes outside of the Airy disk. To find the calibration point, or zero OPD, the subapertures were adjusted until the maximum contrast was realized (though conceptually simple, it is quite difficult to implement). Figure 9 also illustrates the importance of adequate pixilation of the focal plane so that fringes and fringe contrast can be sufficiently measured (i.e., resolved). This differs from standard "pixel versus Airy disk size" trades employed in imaging tasks, which considers pixels smaller than the Airy disk to be useless.

C. Modeling and Control

This section focuses on step 3, maintenance, which means maintaining the calibrated state of the telescope during operation and in the presence of a variety of disturbance sources. The following subsections will motivate on-orbit model validation and system identification and will discuss controller design for the DOT testbed.

1. System Modeling

Developing good models and a rigorous model validation process is critical to achieving the desired structural behavior and control

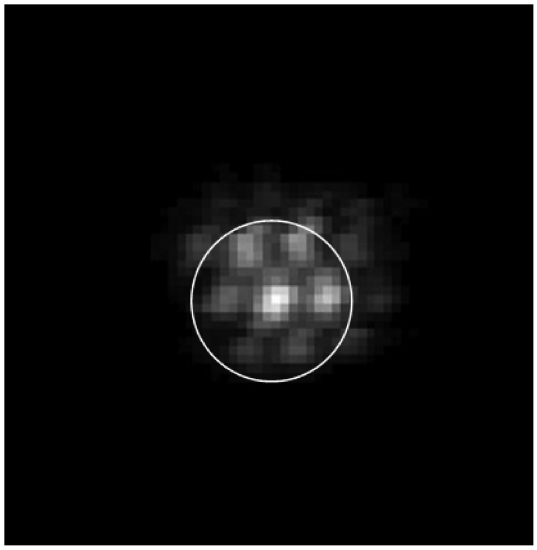

Fig. 9 Measured fringes captured during DOT calibration.

system performance on orbit. Design-related decisions made during the early phases of a program are largely based on models, especially if prior experience on the particular class of payload is not available. Models are used to define actuator and sensor locations, predict amplitudes of motion, and estimate mode shapes. Models must be validated incrementally during development to reduce uncertainty and account for design changes. There are many sources of model uncertainty that can enter into and corrupt a system model. Some important sources of model uncertainty (or error) include 1) nonstructural mass (accounting for cabling, wire harnesses, and insulation); 2) subsystem coupling (bolted joints, interfaces, adhesives, and flanking paths); 3) approximations of boundary conditions (agreement between models and hardware); 4) damping approximations (viscous, hysteretic, frequency, and amplitude dependence); and 5) modeling sensor and actuator dynamics. During testing and model validation, there are also many sources of uncertainty that can reduce accuracy, such as 1) test fixture boundary conditions; 2) unexpected coupling and flanking paths; 3) actuator and sensor dynamics; 4) interference of sensor and actuator hardware with test specimen dynamics; 5) defining appropriate loading conditions (force levels, bandwidth); and 6) technician and procedural errors.

In the case of DOT, structural and optical modeling tools were used extensively during the incremental phases of development. Initial finite element models of the system were developed to insure that the proposed laboratory demonstration had dynamics that were representative of a real spacecraft. Models were updated as the testbed evolved. Because of schedule and budget constraints, validation efforts were limited (unfortunately, this is often the case in spacecraft development). Models were validated against limited modal tests of key components (such as the secondary tower) and with frequency-response measurements. Later, extensive testing of composite materials used on the structure (including statistical analysis of property variation) provided some degree of model improvement [24].

Once the entire DOT system was assembled, a complete finite element model of the telescope was developed (shown in Fig. 10). The model used the geometry of the integrated structure with data, material properties, and damping estimates from component-level tests. The resulting integrated system model included over two million degrees of freedom. However, even this high-fidelity model (developed with significant attention to detail and incorporating prior experience from previous modeling efforts) was only able to roughly approximate the first few low-frequency modes. Figure 11 presents a comparison of a representative model-generated frequency-response function (before any model updating using integrated test measurements) and the corresponding frequency response from a modal test of the integrated telescope. The frequency-response

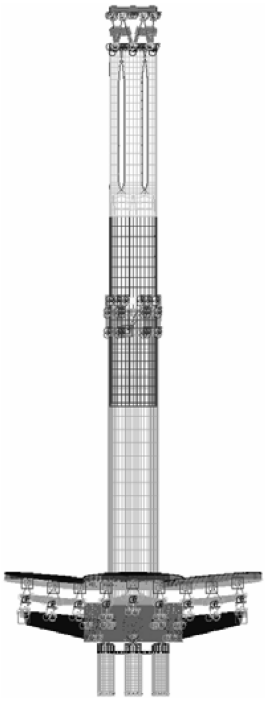

Fig. 10 Finite element model of the integrated telescope.

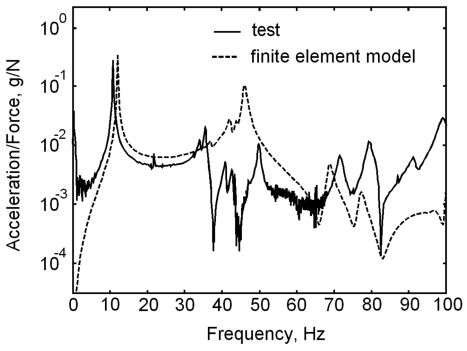

Fig. 11 Comparison of finite element model to test measurement.

functions shown are for an input immediately below the secondary-mirror support structure to a point on the secondary tower above the latch. Table 1 presents some of the results from the modal test.

Thus, on-orbit testing for model validation is required given that prelaunch validation is not always feasible due to the size of the spacecraft, the inability to accurately simulate on-orbit conditions, and the error introduced by gravity offloading (for large deployable systems). Unvalidated spacecraft models offer only gross estimates of on-orbit behavior and deteriorate with increasing frequency and modal density. Models are still useful as engineering tools, but the limitations must be understood. Model utility is improved by quantifying and minimizing model uncertainty.

Models need not be deterministic (such as finite element models). Statistical energy modeling approaches have been used successfully for predicting averaged response levels of structural systems at

Table 1 Data from the modal test of the integrated telescope

Mode	Frequency, Hz	Damping, %	Description
1	10.44	0.53	First tower bending
2	10.85	0.53	First tower bending
3	34.11	0.99	Second tower bending
4	35.50	1.09	Second tower bending
5	44.25	0.87	Tower torsion and first bending
6	46.86	0.60	Tower torsion
7	49.82	0.85	Tower torsion and second bending

higher frequencies. Hybrid modeling tools that combine low-frequency deterministic modeling with statistical approximations for modally dense subsystems have recently become commercially available [25]. Development of one approach for hybrid modeling was accomplished by ESI (formerly Vibro-Acoustic Sciences of San Diego, CA), as part of an Air-Force-sponsored Small Business Innovative Research program.

2. *System Identification*

Controller performance is contingent upon the quality of the system model used for controller synthesis. In system identification, a system model is synthesized from frequency-response-function measurements for a given set of input and output paths. It must be understood that this limited set of transfer function measurements do not necessarily characterize all of the structural dynamics in the given bandwidth. The level of characterization that can be made from system identification data is dependent upon such factors as controllability and observability of the given actuator and sensor set, coupling between the structure and transducers, and spatial and temporal sampling. Consequently, system identification measurements are typically insufficient for model validation (that is, model validation in the sense for which modal testing is used). In practice, model validation in the classical structural dynamics sense is not practical, and only a limited subset of information about the overall system can be inferred from the system identification. Nevertheless, system identification can provide the necessary and sufficient measurements for designing and implementing control laws for complex systems, for which sufficiently accurate analytic or numeric models are not available.

The obstacles in developing high-quality system identification models from data measured on orbit are daunting. For DOT, a wide-bandwidth model (up to 1000 Hz) was necessary to facilitate control system design, simulation, and closed-loop analysis. Modeling low-frequency response was essential to facilitate setpoint control of the optical surfaces. Additionally, model accuracy had to be sufficient at high frequencies to avoid (reduce) controller spillover (i.e., increasing the response amplitude as opposed to reducing the response amplitude). Poles and zeros had to be accurately modeled to achieve the high levels of closed-loop damping needed at lightly damped, low-frequency structural modes that tended to be easily excited by ambient disturbances.

There are many options for system identification of a multi-input, multi-output (MIMO) system. In this work, a frequency-domain modeling approach was used. A key advantage of frequency-domain methods is that band-limited measurements generated in separate tests can be stitched together to form a full-bandwidth transfer matrix. Frequency data need not be uniformly spaced. Often, logarithmic frequency spacing is used when measurements are collected over large bandwidths. For very-high-order systems, models can be identified in separate frequency bands and later combined to form a single model. Another benefit is that each data point in the frequency domain may be the result of significantly averaged time-domain data, thus reducing uncertainty and uncorrelated noise. Also, the excitation signals can be tailored to account for system properties. For example, the input amplitude can be increased to obtain good signal-to-noise-ratio data in and around system zeros or decreased to avoid sensor saturation around system poles.

The frequency-domain observability-range space-extraction (FORSE) algorithm as realized in a version of the DynaMod software was used to develop initial models from measured-frequency-response data [26,27]. The FORSE algorithm is a robust frequency-domain MIMO system identification tool that can identify high-order systems and accommodate nonuniformly spaced frequency data. FORSE can be used with a wide variety of input signals as long as the signals are persistent. In this work, a Schroeder-phase input sequence was selected to maximize the energy applied to the system at each frequency while maintaining low overall input-sequence amplitude [28]. This signal consisted of sinusoids at each frequency of interest combined with the relative phase of each sinusoid selected to minimize the peak amplitude of the overall input sequence. This yielded a flat power spectral density for the input sequence.

After synthesis of an initial model, the tuning process was initiated. Model tuning is a time-consuming process that involves nonlinear optimization combined with engineering judgment and experience. The resulting model is not always better than the starting model. However, deficiencies in the initial model can be corrected through tuning to yield a more accurate match to measured data. For example, model synthesis algorithms have demonstrated difficulty fitting MIMO models exhibiting low-amplitude response at low frequency. A model can be improved in the low-frequency band by tuning with appropriate frequency-weighting matrices. Correlation and error metrics provide powerful tools to improve efficiency and guide the model tuning process [29,30].

3. *Controller Design*

The required control tasks for DOT included 1) maintaining precise mirror alignment and positioning for image quality, 2) suppression or damping of structural vibration, and 3) rejection of persistent disturbances. Additionally, for ground testing, it was recognized that the point source used for calibration would be subject to ambient motion and thermal atmospheric effects not present on orbit. Consequently, this caused line-of-sight error such that tracking of the point source was required to mitigate this effect.

The control system used on DOT was based on a variation of linear-quadratic-Gaussian (LQG) optimal setpoint control [31]. Setpoints for the position of each primary mirror segment were determined during the calibration phase. Low-bandwidth integrator-type control was used to maintain setpoint positions. Upon the low-bandwidth controller, a wide-bandwidth ($\sim$1000 Hz) dynamic output-feedback controller was implemented to provide active damping and wide-bandwidth disturbance rejection. The feedback controller was developed based on MIMO system identification models. Finally, an adaptive disturbance rejection (ADR) controller was applied as an outer loop around the LQG and setpoint controller to target tonal disturbances such as simulated reaction wheel vibration. A simplified block diagram of the system and controller in two-port form is given in Fig. 12. Exogenous disturbances are represented as $w(t)$ and include ambient noise and vibration acting on the system, variations of the index of refraction (sensor noise), and simulated reaction wheel disturbances. Control inputs included the reference setpoints $r(t)$ for each mirror segment, and the structural actuator inputs $u(t)$. Performance metrics $z(t)$ represent the sensed motion of the mirror segments, which was to be suppressed. The performance metrics were the same as the sensed variables, which were the piston, tip, and tilt motion of the three primary mirror segments. Computing the wave-front error increases the computational load and level of controller complexity and was beyond the scope of this phase of the effort. Therefore, wave-front error was not explicitly included as a performance metric in controller design.

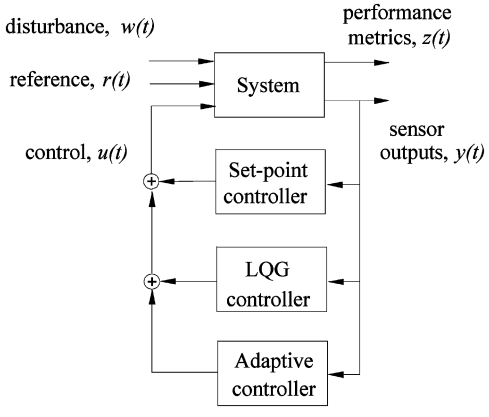

Fig. 12 Block diagram description of the DOT control design.

Design of the LQG controller was straightforward once a system model was generated. The LQG algorithm used the relative weighting of the output vector to the control effort to develop stable and robust control laws. The performance metric is given as

$$J = \int (y^T Q y + u^T R u)\, \mathrm{d}t \tag{2}$$

where Q and R are weighting functions (matrices). Frequency-shaped weighting functions were not necessary on the performance metrics, because the system exhibited a natural rolloff in response with frequency. State-estimator design was accomplished using a similar weighting approach on the sensor-noise input and exogenous-disturbance input.

One significant complication was the need to design and implement several controllers simultaneously to insure a graceful transition in the event that one or more of the sensors failed (i.e., interferometer dropout). To insure stability in the event of sensor failure, the controller verified the status of the sensor signals and implemented the appropriate feedback controller (similar to gain scheduling). This is depicted graphically in Fig. 13. Therefore, several control laws had to be developed, one for each contingency. Switching between control laws was simply a matter of recovering from initial conditions, which reduced the risk of instability, actuator saturation, and equipment damage.

An adaptive controller was implemented to target persistent deterministic disturbances that would not be sufficiently attenuated with the broadband LQG controller. Bus actuators such as reaction wheels can generate strong tonal excitations. These tones propagate through the system and can be measured by the sensors. Let the change in magnitude and phase of the tones due to propagation through the system be represented by the transfer function $T_{yw}(s)$. For a linear system with a stationary disturbance, the sensor output is correlated to the disturbance input. Therefore, a relatively simple control filter can be used to generate a control input to cancel the effect of the disturbance as measured by the sensors. This is depicted graphically in Fig. 14, in which $T_{yu}(s)$ represents the transfer path from the control input to the sensor output. The algorithm can be made adaptive to track changes in the disturbance signal. If $T_{yu}(s)$ is a broadband model (as developed by system identification), then the feedback controller can accommodate changes in the disturbance frequency. This controller does not require a model of the transfer path $T_{yw}(s)$ or a reference measurement of the disturbance input.

Finally, a single-input, single-output adaptive controller was implemented to maintain position accuracy of the white-light point source relative to the telescope [32]. This was necessary because the point source was mounted above the telescope on a metrology tower, which was subject to sway. This was entirely an artifact of ground testing and would not be required on orbit. A small tracking telescope was mounted onto the optics bench to which DOT was mounted. This tracking telescope pointed up at the point source and was vibration-isolated from the optics table to decouple the sensor from floor vibration. Any motion of the point source measured by the tracking telescope was input to an auxiliary controller, which actuated a fast steering mirror in the beam path of the point source.

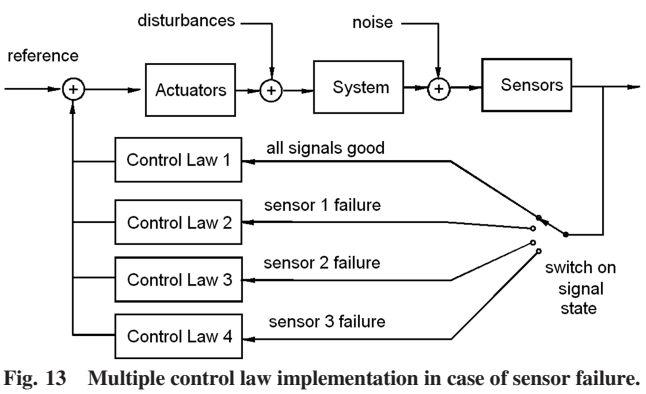

Fig. 13 Multiple control law implementation in case of sensor failure.

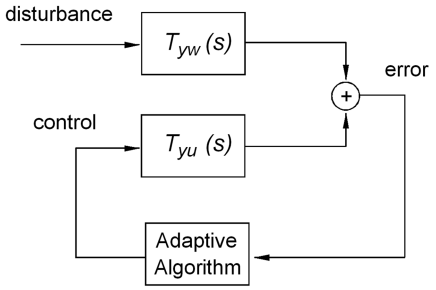

Fig. 14 Block diagram description of the adaptive disturbance rejection controller.

D. Reaction Wheel Disturbance

In addition to demonstrating stable closed-loop control and rejection of ambient disturbances, it was desired to demonstrate that image quality could be maintained when subjected to a simulated reaction wheel disturbance. Reaction wheel disturbances are highly correlated to wheel speed and are dependent upon coupling with the spacecraft and the size (inertia) of the spacecraft. For the DOT testbed, it was determined that for the given mass and inertia, a suitable disturbance input would consist of a primary tonal input at 115 Hz. Five harmonics of this tone are listed in Table 2, which also gives the rms input levels for each harmonic. Testing was accomplished by attaching an electromagnetic shaker to the optics table near the telescope. An accelerometer block (triaxial) close to the disturbance input monitored the input amplitude levels, but was not used by the controller for feedback.

E. Image Quality Assessment Using Twyman–Green Interferometry

A full-aperture wave-front monitoring system was necessary to provide a quantitative indication of the image quality of the closed-loop system, independently of the sensors used for feedback control. The white-light interferometer allowed us to position the mirrors at zero OPD, but provided no quantitative information regarding subsequent phase errors induced by ambient disturbances, the control system, simulated reaction wheel disturbances, or even system variations over time. The heterodyne interferometer and tilt sensors (the interferometer did not provide tilt) only provided information on the dynamic motion of the mirrors at a point on their surface and were limited to rigid-body motions (piston, tip, and tilt).

A double-pass Twyman–Green [23] interferometer was used to provide interferograms of the entire DOT beam path except for the final aft optics focusing lens. This interferometer used the green transition line of the helium–neon laser (wavelength of 543 nm). Simply stated, light from the laser was split into two beams, one that traveled the telescope imaging path and one that was directed to a reference flat mirror. The two beams were then recombined and a lens imaged the DOT pupil onto the focal plane of a charge coupled device (CCD) camera, which measured the intensity distribution of the incident light. The image recorded by the CCD is the superposition of the combined wave fronts, which, for a perfectly

Table 2 Simulated reaction wheel disturbance input levels

Disturbance frequency, Hz	Amplitude, μg rms
40.3	25.0
11.5	3.1
230	0.8
322	0.4
598	0.2
644	0.1

aligned system with no optical aberration or tilt error, would result in uniform pupil intensity. The pupil intensity depends on the relative phase between the two beams.

By slightly tilting the reference flat mirror, an interference pattern, or fringes, can be produced on the focal plane of the CCD. The slight tilt produces an effective phase lag across the beam diameter of the reference reflection, which results in alternating bands of constructive/destructive interference with the other beams on the CCD's focal plane. The amount of tilt determines how many fringes are observed on the focal plane. Any deviation or aberration in the telescope's optics can be observed and quantified by analyzing the fringe pattern.

In the case of DOT, three interference patterns were observed, one for each primary mirror segment (or subaperture pupil) being interrogated. Also, because the wave-front monitoring system was monochromatic (using a single wavelength), the mirror segments had to be phased (i.e., calibrated) within $\lambda/4$ (at 543 nm) of the zero OPD to correctly identify the relationship between fringes of different subapertures. Otherwise, the fringe-order numbers are ambiguous and a reliable piston measurement is not possible. A necessary and reasonable assumption in the following analysis is that the calibration procedure (contrast maximization algorithm) with the white-light interferometer achieved zero-OPD phasing. To quantitatively determine residual or induced phase errors, the software program Quick Fringe [33] was used to analyze interferograms of each subaperture. The resulting Quick Fringe data were used by a Mathcad [34] routine to compute the phase error between subapertures of the closed-loop system.

A simulated interferogram of a perfectly phased DOT with perfect optics (i.e., no aberrations) is shown in Fig. 15 (generated by ZEMAX [35]). The apparent circular cutout (eclipse) represents blockage of the image path by the top of the secondary-mirror support structure. With a perfectly phased system, the interference fringes are straight, evenly spaced, and in phase from one subaperture to another. Being in phase implies that if a fringe in one subaperture is extrapolated so that it extends to another subaperture, it lines up with a fringe in the other aperture and has the same fringe-order number. This is demonstrated by the dashed line in Fig. 15, which shows the alignment of a fringe in subaperture A with a fringe in subaperture C.

1. *Interferogram Analysis*

Wave-front phase information was obtained by reducing interferograms of each subaperture. Although the subaperture interferograms were independently digitized and reduced, the subaperture images had to be part of a single image that contained all three subapertures. This preserved the pupil geometry, which was required so that the position of one subaperture relative to the others could be determined. This was necessary to maintain a common tilt reference direction and magnitude for each subaperture. The information required from each interferogram consisted of the center coordinates of each subaperture, the subaperture radius, and a Zernike polynomial representation of the wave-front aberration function (Zernike polynomials are a set of basis functions that can be used to describe optical wave fronts, and they are analogous to the mode shapes used to model structural vibration). The piston relationship between fringes of different subapertures, represented by fringe-order numbers, is also required and must be defined by the user.

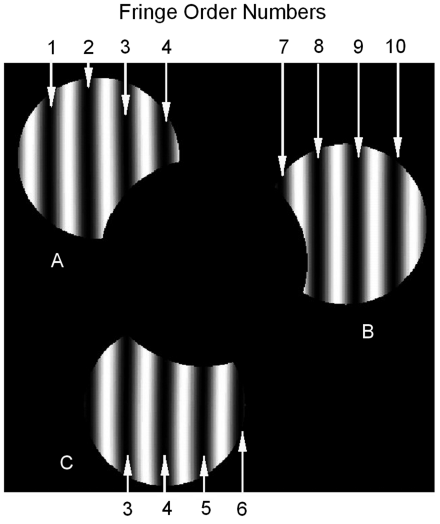

Fig. 15 Simulated interferogram of a perfectly phased DOT.

The fringe-reduction process begins with the user assigning global fringe-order numbers to define how fringes in each subaperture relate to each other. Quick Fringe's automatic fringe-tracing feature was used to create fringe center data points along the fringes. Fringe-order numbers were manually assigned to the fringes based on the global fringe numbering adopted, and then minor adjustments were made to fringe centers when the automated process had difficulties.

The process for determining tilt and piston errors is illustrated graphically in Fig. 16, in which, for clarity, the problem is simplified to one dimension (x represents the distance measured across the pupil). Figure 16a depicts three subaperture wave fronts with local tilt and piston errors, as well as a global tilt component (indicated by the dash-dot line). Global tilt occurs if the entire primary mirror plane is tilted with respect to the pupil plane. First, local tilt in each subaperture was computed and subtracted, yielding Fig. 16b. Next, the global tilt was estimated and subtracted from the measurements, yielding Fig. 16c. With this accomplished, the subaperture piston errors can be estimated. The relatively straightforward calculations are omitted here for brevity.

2. *Example Simulations*

The data-reduction process was implemented in a Mathcad spreadsheet and tested with simulated interferogram cases. The first case used the interferograms in Fig. 15, which modeled a perfectly aligned system with no aberrations; Table 3 lists the results. Ideally,

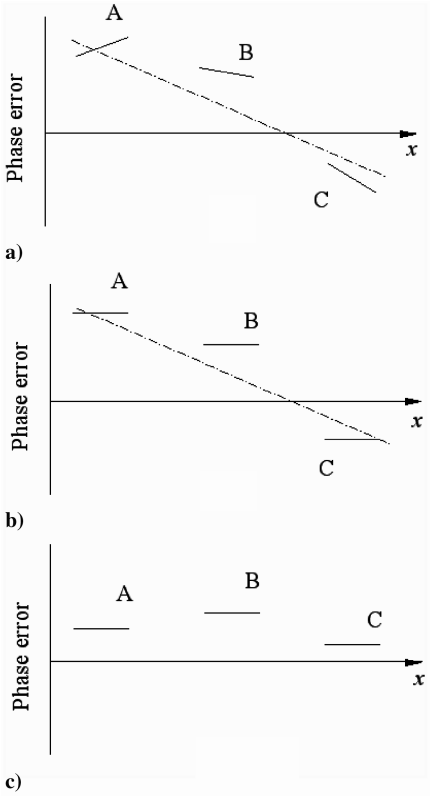

Fig. 16 Finding relative piston errors: a) segment wave fronts with tilt and piston error, b) subaperture tilts subtracted, and c) global tilt removed, leaving subaperture piston (phasing) errors.

Table 3 Reduction of a simulated interferogram of a perfectly phased DOT

Subaperture	Piston error Waves, OPD	nm	Tilt error Waves, OPD/subaperture diameter	nrad
A	0.025	13.58	0.016	17.4
B	−0.031	−16.83	0.017	18.5
C	0.006	3.26	0.015	16.3
rms	0.023	12.63	0.016	17.4

the analysis would have indicated zero rms error. The relatively small residual errors are presumably due to the fringe digitization. This simulation effectively benchmarks the uncertainty introduced by the analysis tool.

Next, Fig. 17 presents a simulated interferogram with 0.25 wavelengths of piston error added to segment C. Also, the tilt of the reference mirror was increased slightly to yield 13 dark bands across the aperture. The reference (dashed) line in Fig. 17 clearly indicates the fringe shift in segment C. The analysis results are listed in Table 4 and indicate a computed piston error on segment C of 0.26 wavelengths, which is only $\lambda/100$ from the correct value. Other piston and tilt errors were relatively small. Real interferograms are more difficult to process, due to aberrations, but these simulations suggest that piston and tilt errors of $\lambda/10$ should be possible to diagnose.

IV. Testbed Description

DOT was fabricated, assembled, and tested incrementally over a six-year period. This section provides design and implementation details of various components of the integrated system, design trades, and justifications. The overall testbed consisted of: 1) the telescope, 2) metrology systems, 3) metrology tower, and 4) supporting electronics. The laboratory and ambient test environment are also discussed.

A. Telescope (Hardware, Materials, Assembly, and Mechanisms)

The telescope, depicted in Fig. 18, included 1) a center hub integrating structure, 2) three deployable petals, 3) three 60-cm primary mirror segments, 4) three coarse/fine actuators per mirror segment, 5) a deployable secondary tower, 6) a secondary mirror, and 7) a secondary-mirror support structure. The telescope was oriented to point upward (as opposed to horizontal) to reduce astigmatic lensing effects resulting from ambient thermal atmospheric striation (i.e., changes in the index of refraction caused by slight variations in air density and composition as a function of height). Overall, the telescope had a 1.7-m encircled diameter with 29% aperture fill. The secondary tower was approximately 3.96 m when deployed. The base of the telescope was attached to an optics table, which was rigidly bolted to the laboratory floor. The telescope mass was approximately 120 kg.

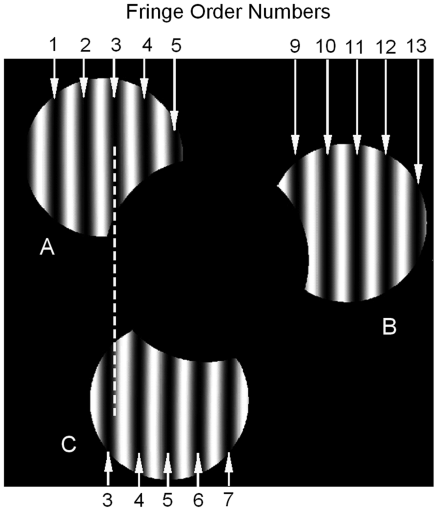

Fig. 17 Simulated interferogram with 0.25λ piston error on segment C.

The deployable optical telescope was designed to be a finite-conjugate design (meaning that it maps a focal point to a focal point, not infinity to a focal point) [23]. The finite-conjugate optical design was driven by a number of cost factors and by early design trade considerations. An infinite-conjugate design would need a full-aperture collimator, which would be expensive and would introduce many practical integration and experimental issues. For this demonstration system, the finite-conjugate design was the optimal solution. Additionally, a spherical prescription (as opposed to aspheric) was decided upon as the best option to reduce risk, cost, and manufacturing time of the primary mirror segments. When incorporating spherical mirror segments into a system-level design, it was found that the aberrations they induced in an infinite-conjugate system would be difficult to mitigate in a space-traceable design. The finite-conjugate design reduced spherical aberrations and allowed for a point source to be used in the laboratory, which is similar to what would be used on orbit.

1. *Integrating Structure*

The hexagonal center hub integrating structure was constructed at the AFRL by the advanced composite structures research and development team using graphite–epoxy composite material. The structure used a balanced layup of

$$[0/45/90/-45/45/0/0/0/0/-45/45/0/0/90]$$

with 0.152-mm-thick layers, which yielded an overall modulus of 172 GPa. The integrating structure provided an interface to the primary mirror petals via two precision hinges and three high-stiffness self-rigidizing latches. The center of the integrating structure was a tapered cylinder designed to join with the secondary tower.

2. *Reaction Plates (Petals)*

Three identical reaction plates, or petals, were also designed and fabricated at AFRL using graphite–epoxy composite. Each was fabricated using a balanced layup of

$$[90/0/0/-45/45/0/0/0/0/-45/45/0/0/90]$$

with 0.152-mm-thick layers, which yielded an approximate elastic modulus of 172 GPa in the radial (longitudinal) direction. The petals resembled tapered boat hulls. At their base, the cross section was triangular, which tapered off to a blunted point approximately 94-mm wide. Aluminum blocks imbedded in the petals provided hard points for mounting hinges, latches, and actuators. As shown in Fig. 19, each petal supported three actuators, an intermediate support plate, a primary mirror segment, and three bipod mirror flexures. The petals were carefully designed such that the mirror centers would be located 550 mm from the telescope centerline. In their deployed configuration, the petals rested at an angle of about six degrees upward from horizontal.

Table 4 Reduction of a simulated interferogram with 0.25λ piston error on segment C

Subaperture	Piston error Waves, OPD	nm	Tilt error Waves, OPD/subaperture diameter	nrad
A	0.009	4.89	0.020	21.7
B	−0.009	−4.89	0.025	27.2
C	0.262	142.27	0.014	15.2
rms	0.151	82.23	0.020	21.9

3. Primary Mirror Segments

The primary mirrors were fabricated by ITT (formerly the Eastman-Kodak Imaging Systems) from ultra-low-expansion glass. Three circular mirror segments were manufactured to have a 5-m radius of curvature and less than 10-nm (rms) surface error. A single mirror (before surface coating and final polishing) is shown in Fig. 20. The critical segment-to-segment radius-of-curvature-matching error was measured to be less than 40 μm. The fabrication procedure used precision water-jetting to create a honeycomb support structure, which resulted in an overall area density of approximately 15 kg/m^2, making these the most lightweight precision ultra-low-expansion mirrors ever fabricated at this diameter (at the time of production). Figure 21 shows all three mirror segments installed on the telescope.

4. Mirror Actuators

The actuator assemblies consisted of a low-voltage piezoelectric stack actuator mounted on a micrometer drive with a dc servomotor.

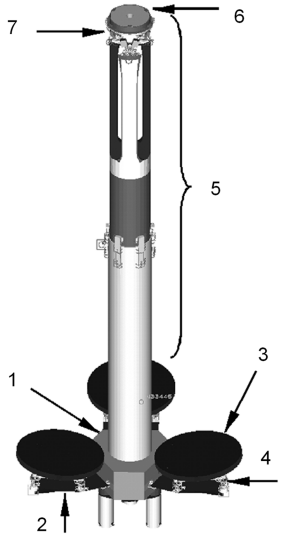

Fig. 18 Solid model rendering of the DOT; 1: center hub integrating structure, 2: deployable petal, 3: 60-cm primary mirror segment, 4: three coarse/fine actuators per mirror segment, 5: deployable secondary tower, 6: secondary mirror, and 7: secondary-mirror support structure.

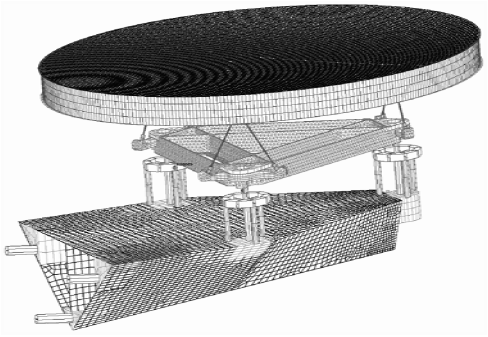

Fig. 19 Finite element model of a single deployable petal with mirror support hardware.

The piezoelectric actuator had a range of 30 μm and a resolution of 1 nm, and it provided high-bandwidth control capability. These actuators were driven by a 100-V analog linear amplifier. The micrometer had a 10-mm range with 60-nm resolution and provided low-bandwidth coarse positioning capability. The resolution of the coarse actuators was obtained using an encoder sensor built into the servomotor, which was commanded by an RS-232 serial interface. Each assembly was attached to the reaction plate by a screw clamp on the micrometer. Figure 22 shows two actuator assemblies attached to the underside of a mirror segment. The actuators were attached to the mirrors by a bipod flexure system that provided a stiff kinematic interface.

5. Deployable Secondary Tower

The secondary tower cantilevered vertically from the integrating hub structure. It used a tube-within-a-tube construction, such that the interior tube was deployed by a cable–pulley actuator system and latched once fully extended. Testing showed deployment repeatability on the order of 1 mm $\pm$ 0.5 mm. The secondary tower was fabricated from graphite–epoxy composite. Additional details regarding the material properties and mechanical behavior of the secondary tower can be found in the thesis by Daniels [24]. The tower had an outer diameter of 300 mm and had elliptical openings spaced at 120 deg at the top to allow light from each primary mirror to

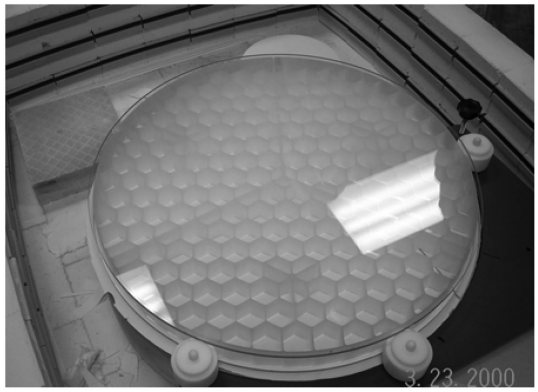

Fig. 20 Lightweight 60-cm mirror segment before coating.

Fig. 21 All three primary mirror segments installed on the telescope testbed.

Fig. 22 Coarse and fine actuators used to position mirror segments.

impinge on the secondary mirror. The overall length of the secondary tower was 3.96 m.

The fundamental modes (cantilever) of the secondary tower were very lightly damped and susceptible to excitation by distant street traffic and the building's air-handling systems. Although the vibration amplitude was small, it still had a detrimental effect on the experiment. Therefore, it was necessary to add a piezoelectric patch actuator pair to the base of the secondary tower to provide authority to control tower motion.

6. Secondary Mirror and Support Structure

The secondary mirror was attached to the top of the secondary tower by a hexapod support stand. The secondary mirror had a radius of curvature of approximately 1.36 m and was about 29 cm in diameter. The separation between the primary and secondary mirrors was about 3.6 m. The hexapod was capable of being actively driven for coarse alignment (less than 1-Hz bandwidth); however, it was used only to provide passive support for the secondary mirror during these experiments. The secondary-mirror support structure also supported three additional 2.5-cm reflectors used by the heterodyne interferometer and tilt sensors' beam paths.

B. Metrology Systems

Three metrology systems were integrated into the DOT experiment. In each case, it was desired to leverage commercially available approaches to avoid development and prototype costs. First, DOT's segmented imaging path operated as a white-light interferometer and was used to calibrate the telescope (initial alignment). Second, a heterodyne laser interferometer system (633 nm) was used to measure the piston of the individual beam paths. The interferometer laser also provided the source for the tilt sensors' beam paths. The interferometer and tilt sensors provided sensor inputs to the controller for feedback control to maintain the initial conditions established by the white-light interferometer. Finally, a Twyman–Green wave-front monitoring system (543 nm) was integrated to measure wave-front error.

The white-light interferometer used a 75-W xenon arc lamp as the light source. The lamp was spectrally filtered to limit its bandwidth from about 485 to 650 nm, which increased the effective coherence length of the light. To make a point source, the lamp was spatially filtered by blocking the light with a barrier, allowing transmission to the telescope only through a small pinhole in the blocking material. To maximize light through the pinhole, the source was focused onto the pinhole using a commercially available lens. Inserting the pinhole spatial filter improved the contrast of the white-light interference fringes by reducing spatially incoherent light, but the pinhole also reduced the intensity of the light reaching the imaging camera. It was found that a 5-mm pinhole provided the best compromise between contrast and intensity.

The white-light source was located on an optical bench about 5.5 m above the primary mirror, supported by the metrology tower. The light from the pinhole passed through a zero-power meniscus lens with surfaces concentric to the pinhole that retroreflected

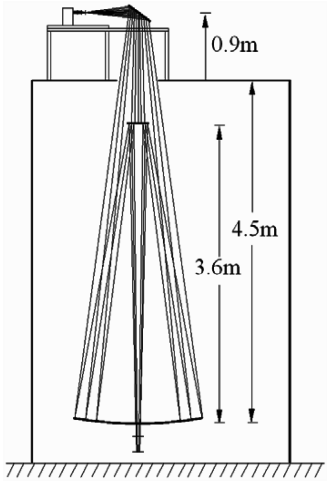

Fig. 23 Illustration of the white-light interferometer setup.

543-nm light from the Twyman–Green interferometer. A fast steering mirror after the meniscus compensated for metrology tower motion and directed light from the pinhole down into DOT's imaging path. A simplistic illustration of the configuration is shown in Fig. 23.

The heterodyne interferometer, a Hewlett-Packard 5507 Laser Position Transducer system, was mounted on the same optics table to which the telescope was attached. The system used a helium–neon laser operating on a magnetically Zeeman-split transition to provide two slightly different orthogonally polarized wavelengths. Beam splitters divided the light between test and reference legs, with local mirrors retroreflecting the reference beam. The test beams passed through pupil imaging and wave-front curvature-matching optics before being retroreflected by the primary mirror segments. The two wavelength laser provided a heterodyne interferometric measurement, which measured changes in position by monitoring the Doppler shift of the interference beat frequency [mirror motion produced a Doppler (frequency) shift in the return beam relative to the reference beam; interference of two beams of nearly the same frequency produced the beating phenomenon from which piston motion was inferred]. The system provided resolution better than 10 nm and a range of 20 m. A single laser source was used, which was split into three separate beams of equal amplitude, one for each primary mirror path. To measure tip and tilt motion of the primary mirror segments, a portion of the return beam from each leg of the interferometer was split off and focused on photopotentiometers. This effectively mapped the angular motion of the primary mirrors to displacements on the photopotentiometers. The photopotentiometer transducers provided two output voltages, which corresponded to the tip and tilt motion of the mirror segment.

The Twyman–Green wave-front monitoring system was also mounted on the optics table to which the telescope was attached. It used a single laser source, which was split to a reference mirror and to the telescope imaging path. The interferometer beam was injected into the DOT imaging path using a dichroic beam splitter located in the collimated space between the two aft optics imaging lenses. The DOT pupil plane defined by the primary mirror segments was imaged onto the interferometer's CCD camera. The heterodyne and Twyman–Green interferometer layout and tilt sensors can be observed in Fig. 24. Although exposed in Fig. 24, the optics pathways were enclosed to eliminate air turbulence and to provide a barrier against thermally induced distortion.

C. Metrology Tower

A steel metrology tower was built around the telescope to support the overhead white-light source. It was designed to be extremely rigid and to support the overhead optics without introducing any significant dynamics. Even so, it was necessary to integrate a white-light monitoring system to correct for very-low-amplitude tower motion. Plastic shielding was attached to the metrology tower

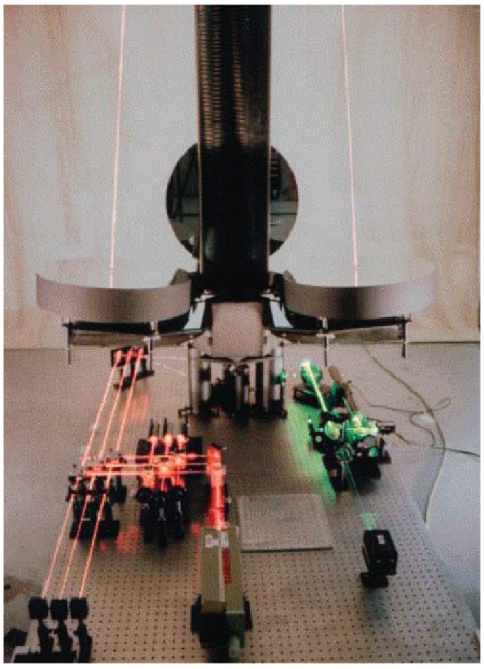

Fig. 24 Heterodyne and Twyman–Green interferometer layouts used on DOT.

to provide additional isolation from the laboratory environment. The metrology tower is shown in Fig. 25.

D. I/O Architecture

The control system was based on a Digital Equipment Corporation system obtained from dSPACE, Inc. This system included a 500-MHz 64-bit Alpha processor and a Texas Instruments TMS320C40 digital signal processor for management of all I/O functions. The system had 32 analog input and output channels, one 96-bit and one 32-bit parallel digital I/O board, and four RS-232 communication ports. The dSPACE system offered tremendous flexibility through the use of MATLAB/Simulink software tools and Real Time Workshop code-generation tools available from MathWorks [36].

Fig. 25 Photograph of the telescope, metrology tower, and overhead optics support structure.

A custom image processing system was used to analyze frames from the white-light interferometer and to determine the calibration setpoints. The image processor was based on the Silvertip-Quad Sharc system from BittWare Research Systems. This system used four 40-MHz Sharc processors from Analog Devices. Processing tasks were distributed among the four processors to provide high data throughput.

The heterodyne interferometer and tilt sensors comprised the entire feedback sensor suite for control experiments. There were three measurements per primary mirror segment (piston, tip, and tilt), for a total of nine sensor signals. The digitized and sampled piston measurements were ported directly to the dSPACE controller. Measurements from the photopotentiometers were antialiased and discretely sampled at the controller sample frequency. There were ten control actuators, three actuators per primary mirror segment, and a piezoelectric patch pair attached to the base of the secondary tower. Additionally, power amplifiers and signal conditioners were used on all I/O channels, as appropriate. All controller hardware, computers, power amplifiers, and signal conditions were set up in the DOT control room, adjacent to the DOT laboratory. Cabling was routed to the telescope through a cable port in the lab wall.

In summary, the controller consisted of 9 sensor inputs and 10 actuator outputs and was executed at a sample rate of 2 kHz. An actual flight system would use application-specific hardware designed for the space environment and to minimize size, weight, and power requirements. However, as the following results will show, a 2-kHz sample rate provides ample bandwidth for a structural control architecture, as demonstrated in this work.

E. Laboratory Description/Environment

The DOT laboratory was designed and constructed to provide the highest degree of isolation from ambient disturbances for developing and testing precision space technology. The dimensions of the lab were $12 \times 12 \times 23$ m, using a box-within-a-box construction with double walls, with a 0.45-m air gap to provide isolation from the surrounding structure. Separate 23-m-deep piers supported the structural steel of the walls, which were constructed of 10-cm reinforced concrete. The inner roof was 0.25 m thick, and the outer roof was 0.45 m thick.

The entire optical system, including the metrology tower and telescope, was attached to an $8.5 \times 9.75 \times 3$ m seismic pad within the lab. The pad was isolated from the surrounding laboratory floor by a 10-cm gap. This concrete pad was produced as a monolithic pour with reinforcing rebar throughout and in all three axes. The concrete pad weighed about 500 t and rested on a 1.5-m-thick bed of compacted gravel.

This provided a very stable and isolated platform for experiments. However, ambient vibration during the day resulting from traffic, the building's air-handling system, and a power transformer located near the lab required experiments to be conducted at night. Ambient vibration during the day excited lightly damped modes of the metrology tower and of the telescope's deployable secondary tower, which swamped the simulated reaction wheel disturbances, caused the interferometers to lose lock and prevented a space-traceable experiment. A triaxial block of accelerometers (PCB 393B31) was placed on the DOT aft optics bench at the base of the telescope (see Fig. 26) to record the typical ambient vibration observed during testing (0300–0400 hrs). Accelerometer signals were sampled at 2 kHz and filtered with a sixth-order low-pass filter with cutoff frequency of 300 Hz (measurements below 300 Hz had at least $\pm 10\%$ accuracy for the PCB 393B31, according to manufacturer specifications). The resulting rms of the acceleration measurements is listed in Table 5. Figure 27 presents the spectrum of the root sum square (rss) of the three accelerometer measurements.

The ambient temperature in the laboratory, which affected the optical index of refraction, exhibited slow variations (± 0.24°C or ± 0.5°F) during the day. Typically, the temperature was more consistent at night (2200 through 0500 hrs). Over an entire year, the ambient temperature varied between 21°C (January) and 29°C (July). The lab was equipped with its own air-handling system, but it

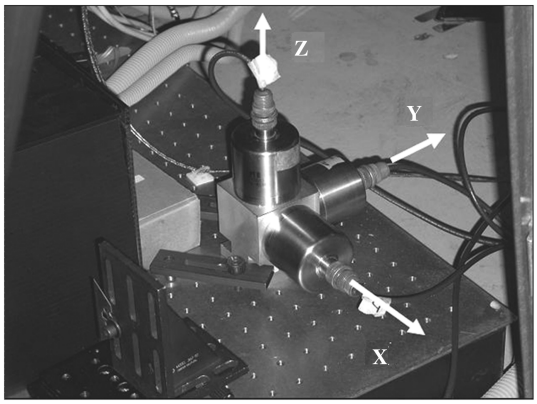

Fig. 26 Triaxial accelerometer block mounted to the DOT optics bench.

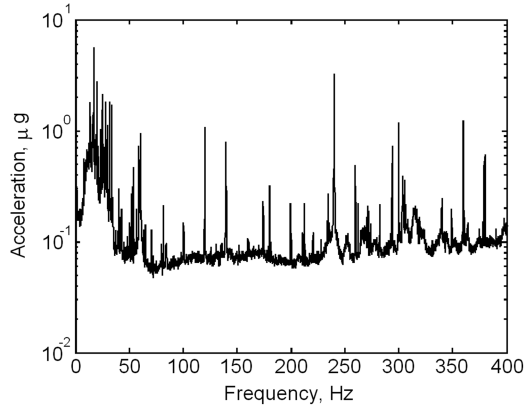

Fig. 27 Spectral content of ambient acceleration (rss).

was not used. Because the variation was small during a 24-h period, it was better to let the ambient air naturally striate in horizontal thermal layers. The air-handling systems would introduce turbulence and constant fluctuations in the index of refraction and would possibly deposit particles onto the primary mirror segments.

The relative humidity in the lab was also measured. The relative humidity in the laboratory varied between 10 and 30% during a year, with an average value of about 24%. However, the degree to which variations in humidity affected composite components is unknown.

V. Results/Analysis

A. System Identification

A key obstacle for system identification on DOT was the large-amplitude discrepancy between on-segment transfer functions and cross-segment transfer functions. "On-segment" means that sensor measurements (piston, tip, and tilt) were of the mirror being actuated. "Cross-segment" means that measurements were of mirrors not being directly actuated (i.e., measuring mirror A's piston, tip, and tilt when actuating mirror B). There was a nearly 2000:1 difference in the rms response levels in the frequency-response-function transfer matrix. On-segment measurements were very good, having little uncertainty, whereas cross-segment measurements were prone to signal-to-noise problems.

Figure 28 presents a measured on-segment frequency-response function. To evaluate the quality of the frequency-response function resulting from the measured data, the 99% confidence interval was computed at each complex data point and is also shown in Fig. 28. There were some frequencies at which the lower bound tended toward zero, particularly at the fundamental tower mode, but overall, the data appeared very good. Above 500 Hz, there was more uncertainty in the measurement, likely due to a lower signal-to-noise ratio.

Upon successful data collection, a state-space model was synthesized for the full-bandwidth 10-input by 9-output system using the FORSE algorithm and DynaMod tool. After several iterations, a 344-state model was developed. Rather than comparing the measured data with the identified model for each transfer function path, model correlation will be inferred by comparing principal gain plots. Figure 29 compares the maximum singular values of the measured data and the identified model. Subsequent plots, Figs. 30–32, present all nine principal gains for different bandwidths. Overall, there was good agreement between this model and measured data. The three dominant principal gains exhibited good agreement through 700 Hz. Above 700 Hz, there were some small discrepancies. The other six principal gains of the model tracked the data reasonably well through 200 Hz, with the exception of some apparent measurement uncertainty about 140 Hz. At higher frequencies, there was more measurement uncertainty in the lower-amplitude principal gains and therefore less agreement. Additional details on DOT data collection, system identification, and observed amplitude-dependent nonlinearities can be found in the paper by Lacy et al. [37].

Table 5 Measured ambient base acceleration

	Acceleration, μg rms
X axis	17.37
Y axis	26.97
Z axis	19.48

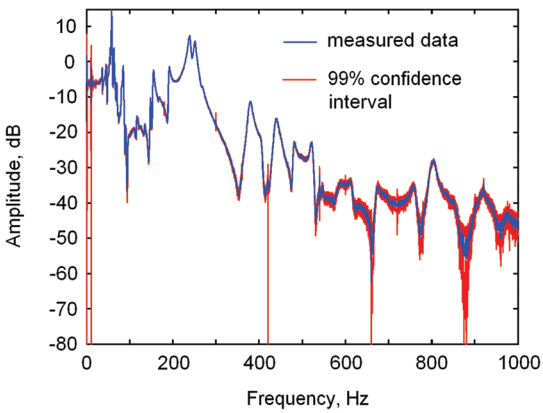

Fig. 28 DOT frequency-response function with 99% confidence interval.

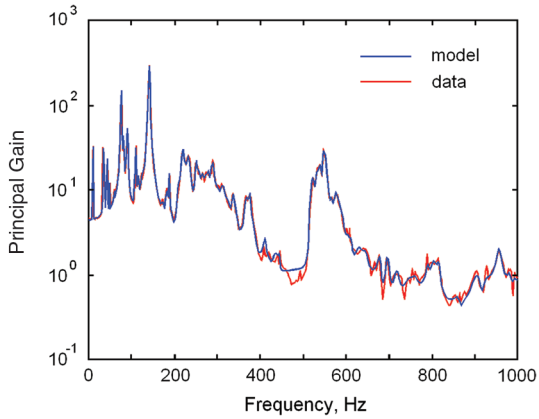

Fig. 29 Comparison of maximum principal gain for the full-order DOT model and measured data.

B. Vibration Control

Using the system identification model, a full-order (344-state) LQG optimal output-feedback controller was designed and used to close the loop on DOT. This controller did not incorporate the adaptive disturbance rejection loop for persistent disturbances. The

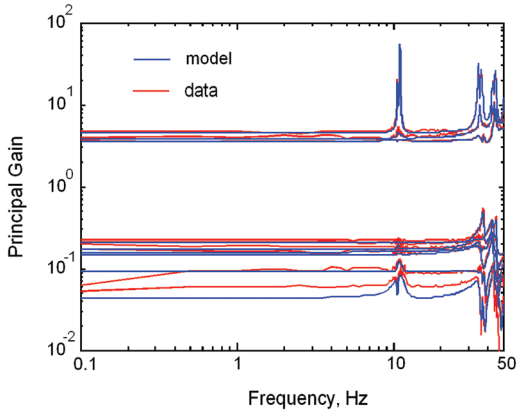

Fig. 30 Comparison of principal gains over 0.1 to 50 Hz.

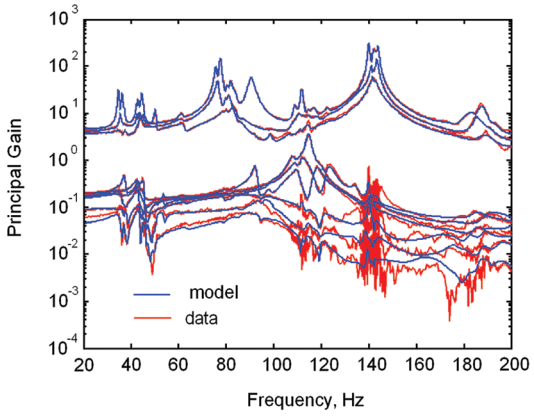

Fig. 31 Comparison of principal gains over 20 to 200 Hz.

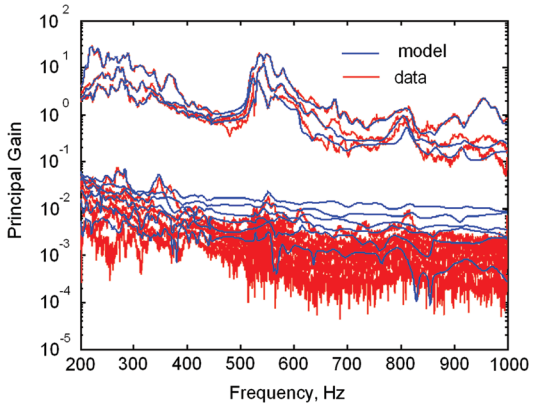

Fig. 32 Comparison of principal gains over 200 to 1000 Hz.

controller was implemented at a 2-kHz sampling frequency. At ambient disturbance levels only, open- and closed-loop sensor measurements were recorded (at a 2-kHz sampling frequency for 300 s). Figure 33 presents the open-loop interferometer measurement for mirror segment C. Note the considerable variation in the open-loop piston measurement over the 300-s interval. Figure 34 presents the closed-loop measurement for the same sensor. This demonstrates that the ability to further reduce piston motion was limited by the quantization level of the sensor and the accuracy limitations introduced into the LQG estimator.

Table 6 lists the open- and closed-loop rms levels. In each case, the rms of the piston motion was reduced. However, reduction of piston motion was often at the expense of increased tip or tilt motion. Some tip and tilt sensors exhibited increased amplitude over particular frequency bands that exceeded reductions achieved at other frequency bands (i.e., control spillover). To illustrate, Fig. 35 shows

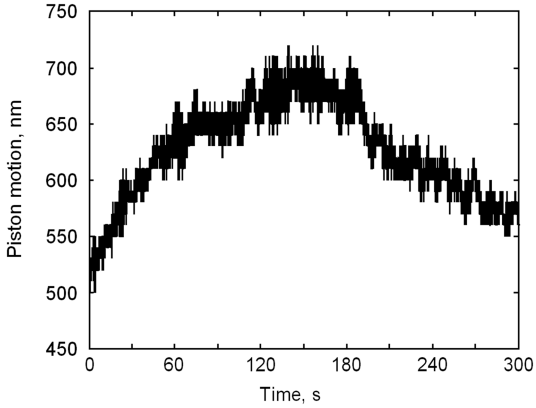

Fig. 33 Open-loop piston measurement for mirror segment C.

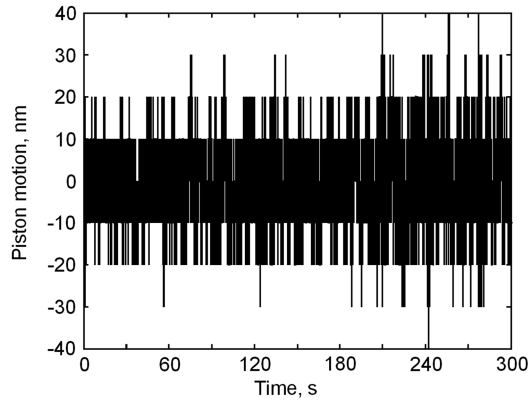

Fig. 34 Closed-loop piston measurement for mirror segment C.

the open- and closed-loop power spectral density plots for tilt motion of mirror segment B. With the exception of the secondary tower modes (about 10 Hz), the closed-loop response from 2 to 40 Hz was greater than the open-loop response. Likely, this resulted from noise in the control loop, because the loop-gain was relatively large over this bandwidth and the sensor levels were so low (less than 20 nrad). Because we are not comparing the gain of the open-loop to closed-loop frequency-response functions, but measured rms levels of the measured sensor data, some of the discrepancy could result from variations in the ambient disturbance environment during testing.

Figures 36–38 present the cumulative sum of the rms contribution as a function of frequency for each piston measurement. These plots show that the largest dynamic contribution (both open and closed loop) was the motion of the secondary tower. Consequently, damping of the secondary tower mode accounted for most of the realized rms reduction across the bandwidth.

Figure 39 shows representative open-loop and closed-loop frequency-response functions between the piezoelectric patch actuator at the base of the secondary tower and the piston response measured at mirror A. In the open-loop plot, the two closely located

Table 6 Open-loop and closed-loop rms values obtained from the LQG controller

Degree of freedom	Open loop (rms)	Closed loop (rms)
Piston A	11.62 nm	7.37 nm
Tip A	12.90 nrad	15.86 nrad
Tilt A	12.01 nrad	9.13 nrad
Piston B	13.91 nm	6.63 m,
Tip B	11.71 nrad	18.85 nrad
Tilt B	14.87 nrad	15.90 nrad
Piston C	9.01 nm	7.59 nm
Tip C	12.05 nrad	16.96 nrad
Tilt C	9.08 nrad	8.62 nrad

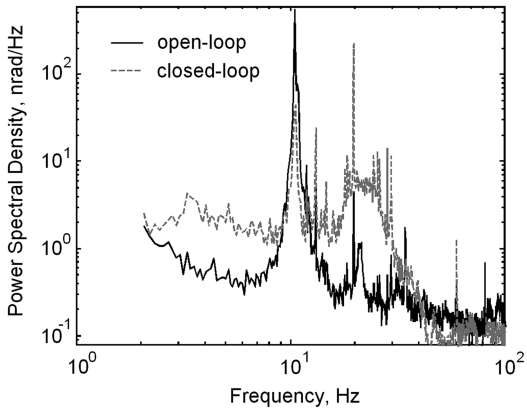

Fig. 35 Power spectral density of mirror-B tilt motion.

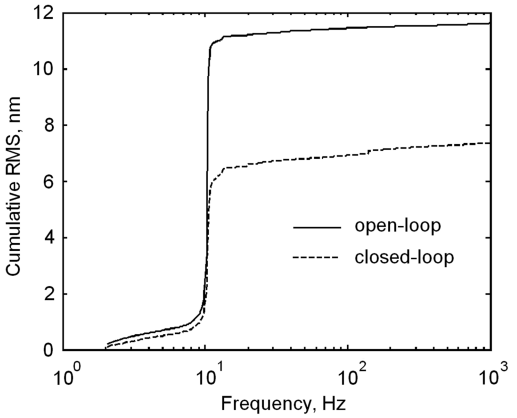

Fig. 36 Cumulative rms of piston measurement for mirror A.

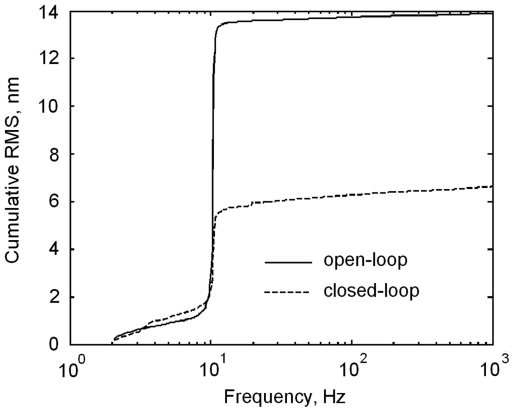

Fig. 37 Cumulative rms of piston measurement for mirror B.

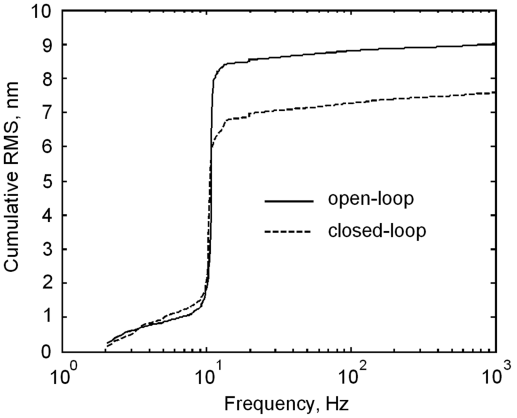

Fig. 38 Cumulative rms of piston measurement for mirror C.

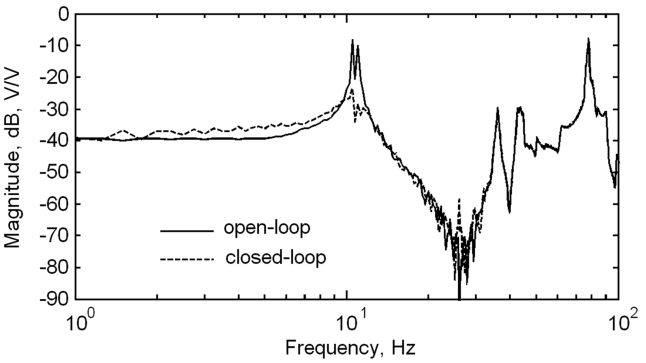

Fig. 39 Frequency-response functions from the piezoelectric patch actuator to mirror A.

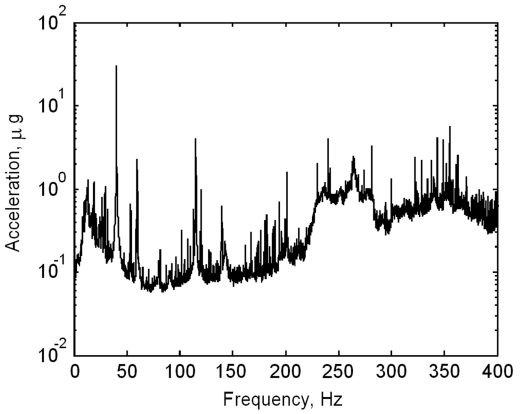

Fig. 40 Spectral content of base acceleration (rss) with simulated reaction wheel disturbance.

resonance frequencies near 10 Hz can be observed. Figure 39 indicates an approximately 15-dB reduction of the response at about 10 Hz: approximately one-sixth of the open-loop amplitude.

The next control tests used the simulated reaction wheel disturbance input. To augment the controller with the ADR loop, the order of the controller had to be reduced to 100 states, which was accomplished using a balanced system reduction based on Hankel singular values. This controller was also implemented using a 2-kHz sampling frequency. Figure 40 presents the rss of the acceleration measured at the base of DOT by the accelerometer block shown in Fig. 26. The presence of the first two tones (40 and 115 Hz) can be easily identified. It was not possible to measure the open-loop mirror responses with the reaction wheel disturbance, because the induced motion exceeded the dynamic range of the sensors. Therefore, the reduced-order LQG controller was used to close the loop on DOT under ambient conditions first, then the simulated disturbance was introduced. Mirror responses were then measured (300 s). Next, the adaptive disturbance rejection loop was turned on, and the mirror motion was remeasured (also for 300 s). Table 7 summarizes the rms

Table 7 Closed-loop rms values with simulated reaction wheel assembly disturbance input

Degree of freedom	Closed-loop baseline controller	Closed-loop disturbance rejection controller (rms)
Piston A	15.30 nm	11.39 nm
TIP A	22.84 nrad	12.74 nrad
Tilt A	83.21 nrad	16.74 nrad
Piston B	29.71 nm	12.82 nm
Tip B	24.90 nrad	79.75 nrad
Tilt B	50.29 nrad	30.51 nrad
Piston C	12.64 nm	8.59 nm
Tip C	47.93 nrad	19.16 nrad
Tilt C	70.65 nrad	18.94 nrad

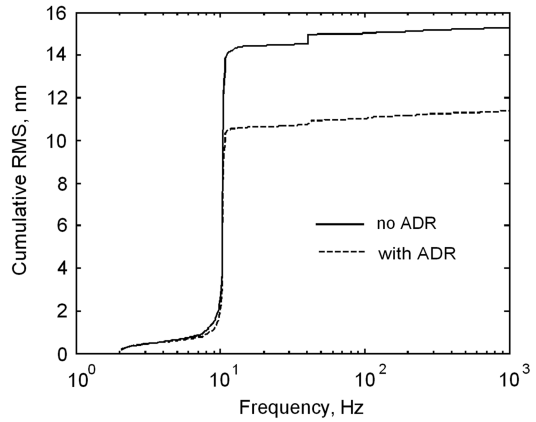

Fig. 41 Cumulative rms of piston measurement for mirror A with simulated reaction wheel disturbance input.

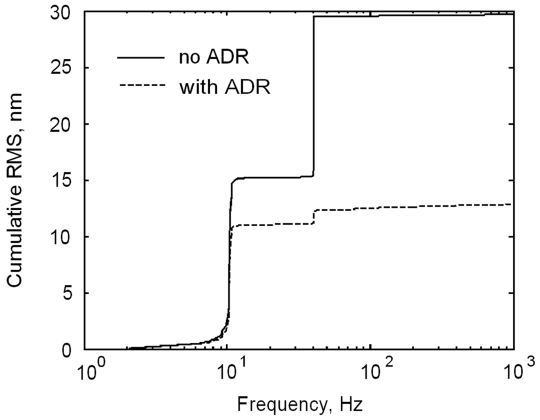

Fig. 42 Cumulative rms of piston measurement for mirror B with simulated reaction wheel disturbance input.

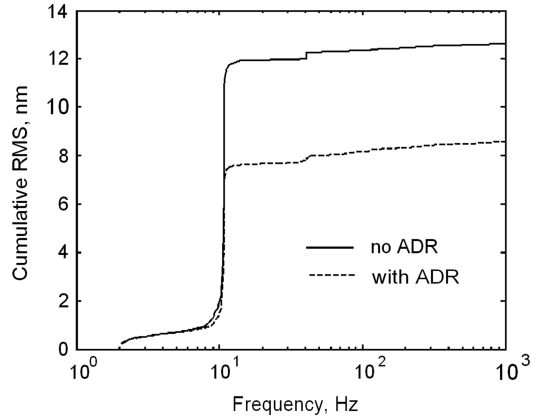

Fig. 43 Cumulative rms of piston measurement for mirror C with simulated reaction wheel disturbance input.

of the mirror piston and the tip and tilt motion. The data indicate that with the reaction wheel disturbance and no ADR controller, the piston motion exceeded the 14-nm rms requirement and approached the 95-nrad threshold on tip and tilt. With the ADR controller, there were significant reductions (except the tip response of segment B). Each segment satisfied the 14-nm rms piston (closed-loop) requirement.

Figures 41–43 present the piston response (cumulative rms) with and without the ADR controller. The data indicate that secondary tower motion was a significant contributor, as in the previous case, and the first subharmonic of the disturbance (at about 40 Hz) was a significant contributor. The other harmonics had little effect on the overall rms level.

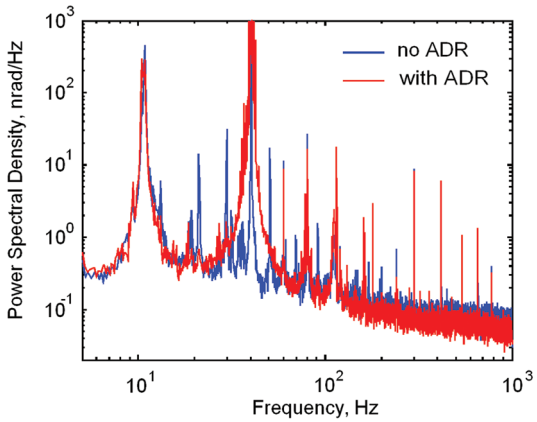

Fig. 44 Power spectral density of mirror B tip motion with simulated reaction wheel assembly disturbance input.

Figure 44 presents the power spectral density plot for the segment-B tip sensor. In spite of reducing several tonal components (12, 20, 30, and 50 Hz), there was a significant amplitude increase at the first reaction wheel subharmonic (about 40 Hz). This was unique to this sensor channel; other channels exhibited reduction across the bandwidth.

C. Wave-Front Error Analysis

Data from the wave-front monitor were collected on DOT with control loops closed (without simulated reaction wheel disturbance). Figure 45 presents a representative interferogram from several that were collected. A reference pattern of equally spaced dashed lines was added to the interferogram to help identify the relationship between subaperture fringes. Identification was complicated by aberrations in the subapertures and by subaperture tilt and piston errors in the DOT system. The reference lines were established with respect to subaperture B (on the right), because it was the least aberrated. The reference lines illustrate that (relative to segment B) segment C (bottom left) had a tilt error, and segment A (top left) had both focus error and some small tilt error. The results of interferogram analysis are given in Table 8. Analysis results indicate that the closed-loop DOT system had a residual rms piston error of 0.168 wavelengths, tip error less than 1/10th of a wavelength, and tilt error of 0.193 wavelengths. The Strehl ratio [38] is also given, which is a function of the rms wave-front error. The closed-loop wave-front error was larger than expected for DOT. Analysis of subaperture interferograms taken at ambient conditions indicated Strehl ratios of about 0.8–0.9 (near diffraction-limited). The reduced closed-loop Strehl was the result of piston and tilt errors between subapertures.

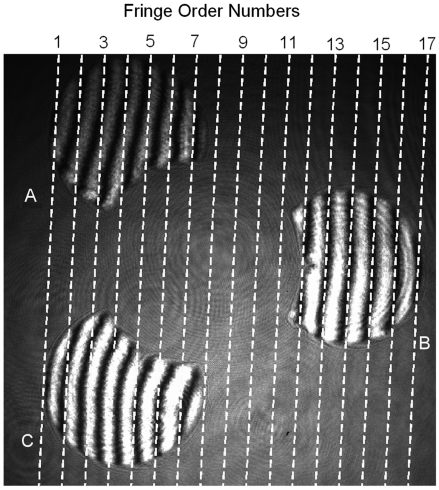

Fig. 45 Closed-loop DOT interferogram.

Table 8 Wave-front errors at 650 nm due to phasing errors relative to mean values

Degree of freedom	Subaperture error (wavelengths) A	B	C	rms error Wavelength		Strehl ratio
Piston	0.182	0.041	−0.224	0.168	109.4 nm	0.327
Tip	−0.119	−0.004	0.073	0.085	110.3 nrad	0.753
Tilt	0.265	0.078	0.187	0.193	250.4 nrad	0.231

D. Imaging

To qualitatively demonstrate image quality, Fig. 46 presents an image taken of a standard Air Force bar target. The bar target replaced the pinhole in the optical path and was illuminated by the xenon lamp. This image was collected on DOT with control loops closed (without the simulated reaction wheel disturbance). This measurement was taken the last day of the period of performance of the effort, and so there was no time to measure "before and after" images with the disturbance sources activated. This picture demonstrates that this sparse-aperture deployable telescope with all of the invasive controller and metrology hardware can indeed be used for imaging. Because the bar chart is not calibrated, no quantitative results can be inferred. The photo was a little dark on the left, the result of not focusing the xenon lamp onto the center of the slide. There were no apparent aberrations, and the contrast looks sharp. The clarity appears quite good, especially considering that the image replaced a 5-μm pinhole. When asked if image quality was as expected, we must refer to the interferogram analysis and the computed Strehl ratios, which (for the few measurements taken and analyzed) were below our expectations.

VI. Conclusions

The deployable optical telescope was an integrated experiment of a space-traceable deployable telescope design with realistic metrology and calibration systems, composite structural components, and lightweight primary mirror segments. This research effort focused on 1) understanding the behavior and modeling of complex precision space structures, 2) developing and demonstrating suitable system identification tools, and 3) demonstrating wideband active control to suppress structural vibration and maintain image quality while subjected to simulated spacecraft disturbances. Many critical aspects of designing and operating a large deployable space telescope were presented, including postdeployment capture, calibration of the imaging system, and maintaining image quality during the mission life.

A key finding of this work was the importance of modeling and the difficulty in achieving accurate integrated system models. It was shown that predictions from high-fidelity models (i.e., finite element analysis) constructed with great attention to detail can significantly deviate from the behavior of the actual integrated system. The dominating effect of the secondary tower motion was not identified in early models and, consequently, piezoelectric patch actuators had to be added to the tower base to provide sufficient control authority. Models should be experimentally validated during the manufacturing and assembly stages to maintain accuracy. The model is the first reference checked when anomalies occur.

Fig. 46 Closed-loop image of a standard bar target.

On-orbit system identification and controller tuning capability must be anticipated and included in the development of a tactical space telescope design. The work presented here focused on frequency-domain system identification. State-space models were synthesized that agreed with experimental measurements over three frequency decades (1 to 1000 Hz). Long data sets were required to provide sufficient averaging needed to reduce noise effects and to provide the necessary frequency resolution of the closely spaced lightly damped secondary tower modes. One particular challenge was the wide dynamic range observed between on-segment and cross-segment measurements. Thermal beam steering introduced low-frequency error. Modeling high-frequency behavior was difficult due to the low signal-to-noise ratio. Over the course of the research effort, time-varying system dynamics were observed, as were several forms of nonlinearity; therefore, models had to be regenerated periodically.

There were many challenges to testing such a system in a 1-g terrestrial environment. Design trades, particularly in optic prescriptions and metrology system implementation, were required to control cost and yet keep the experiment space-traceable. Experimental errors were introduced from the test setup that would not be found on orbit, such as motion of the point (light) source used for calibration or sagging effects due to gravity acting on the deployable petals. The laboratory environment was a critical factor, because even low-level ambient vibration and thermal effects had significant impact on the very sensitive measurements. There were also many challenges involved in implementing multiple controllers, data acquisition systems, and diagnostic sensors simultaneously.

Test results indicated successful closed-loop control over a wide bandwidth, meeting the dynamic control requirement for piston and tip/tilt motion of the primary mirror segments for the prescribed simulated disturbance levels. Multi-input, multi-output LQG controllers were able to reject ambient motion to sensor-noise levels. It was observed that the response of the secondary tower was the most significant contributor to mirror motion across the bandwidth (1000 Hz). The LQG controller was able to reduce the amplitude of the tower motion by approximately 15 dB, which afforded the greatest rms reduction in primary mirror motion.

The LQG controllers were subsequently reduced in order (to about 100 states) to allow simultaneous implementation of an adaptive disturbance rejection loop for narrowband persistent control. The reduced-order controller with adaptive disturbance rejection provided good performance across the bandwidth. With the simulated reaction wheel disturbance, the controller was able to maintain segment piston motion to less than 13 nm and tip/tilt motion to less than 31 nrad, with the exception of one channel.

A full-aperture wave-front monitoring system was developed and integrated to measure the imaging quality of the telescope. This system allowed observation of optical aberrations, possible alignment or phasing problems, and residual control errors. Although dynamic structural motion was controlled to tolerances, the measured wave-front error was larger than desired. This was the result of noncommon optical elements between the imaging and diagnostic beam paths (i.e., noncommon path controller and wave-front monitoring systems).

The AFRL Large Deployable Optics research program ended in September 2005, but not before conclusively demonstrating the ability to accurately control the primary mirror segments of a deployable telescope in the presence of simulated spacecraft disturbances. This testbed provided an unprecedented opportunity for investigating and understanding engineering challenges for developing and testing precision deployable structures. Because of funding and schedule constraints, we were not able to continue interferogram analysis and to attempt to improve image quality, pursue validation of integrated optomechanical system modeling tools, or implement a phase-diversity wave-front sensing and control approach. Thus, there remain many fascinating research avenues to be explored.

Acknowledgments

Sandia is a multiprogram laboratory operated by Sandia Corporation, a Lockheed Martin Company, for the U.S. Department of Energy's National Nuclear Security Administration under contract DE-AC04-94AL85000. Partial support for this project was provided by the U.S. Air Force Office of Scientific Research. The authors would like to acknowledge the contribution and express their appreciation to the following people for their contribution to this effort: Jordan Johnson, Doug Coombs, and Jim Goodding of CSA Engineering for finite element modeling, modal testing and model validation support and Jim Hanson for hardware development and mechanical engineering support. Finally, we would like to acknowledge the many contributions in system identification, modeling, and control analysis made by several space scholars during the course of this effort.

References

[1] Warren, P. A., Peterson, L. D., and Hinkle, J. D., "Sub-Micron Mechanical Stability of a Prototype Deployable Space Telescope Support Structure," *Journal of Spacecraft and Rockets*, Vol. 36, No. 5, Sept.–Oct. 1999, pp. 765–771.

[2] Plante, R. L., "Large Active Mirror Program (LAMP)," *SPIE Conference on Active and Adaptive Optical Components*, edited by M. A. Ealey, Vol. 1543, Society of Photo-Optical Instrumentation Engineers (International Society for Optical Engineering), Bellingham, WA, 1991, pp. 146–160.

[3] Cox, C. D., and Furber, M. E., "4-Meter Diameter Adaptive Optical System Technology Demonstration," *Space Telescopes and Instruments IV*, edited by P. Y. Bely and J. B. Breckinridge, Proceedings of SPIE—The International Society for Optical Engineering, Vol. 2807, Society of Photo-Optical Instrumentation Engineers (International Society for Optical Engineering), Bellingham, WA, 1996, pp. 132–141.

[4] Carrier, A., and Aubrun, J., "Modal Characterization of the ASCIE Segmented Optics Testbed: New Algorithms and Experimental Results," *Controls for Optical Systems*, edited by J. A. Breakwell, Proceedings of SPIE—The International Society for Optical Engineering, Vol. 1696, Society of Photo-Optical Instrumentation Engineers (International Society for Optical Engineering), Bellingham, WA, 1992, pp. 193–208.

[5] Rather, J. D. G., "NASA's Daughters: SELENE, PAMELA, and NAOMI," *Laser Power Beaming II*, edited by H. E. Bennett and R. D. Doolittle, Proceedings of SPIE—The International Society for Optical Engineering, Vol. 2376, Society of Photo-Optical Instrumentation Engineers (International Society for Optical Engineering), Bellingham, WA, 1995, pp. 11–20.

[6] Ames, G. H., Howard, R. T., Lindner, J. L., Montgomery, E. E. IV, Patterson, A. F., Rakoczy, J. M., Zeiders, G. W., Jr., and Waites, H. B., "PAMELA: Phase I Testing and Verification on a 0.5-m Diameter Telescope with a 36-Segment Adaptive Primary Mirror," *Laser Power Beaming II*, edited by H. E. Bennett and R. D. Doolittle, Proceedings of SPIE—The International Society for Optical Engineering, Vol. 2376, Society of Photo-Optical Instrumentation Engineers (International Society for Optical Engineering), Bellingham, WA, 1995, pp. 160–177.

[7] Rakoczy, J. M., Montgomery, E. E. IV, and Lindner, J. L., "Recent Enhancements of the Phased Array Mirror Extendible Large Aperture (PAMELA) Telescope Testbed at MSFC," *Telescope Structures, Enclosures, Controls, Assembly/Integration/Validation and Commissioning*, edited by T. A. Sebring and T. Andersen, Proceedings of SPIE—The International Society for Optical Engineering, Vol. 4004, Society of Photo-Optical Instrumentation Engineers (International Society for Optical Engineering), Bellingham, WA, 2000, pp. 352–362.

[8] Acton, D. S., Atcheson, P. D., Cermak, M., and Kinsbury, L. K., "James Webb Space Telescope Wave-Front Sensing and Control Algorithms," *Optical, Infrared and Millimeter Space Telescopes*, edited by J. C. Mather, Proceedings of SPIE—The International Society for Optical Engineering, Vol. 5487, Society of Photo-Optical Instrumentation Engineers (International Society for Optical Engineering), Bellingham, WA, 2004, pp. 887–896.

[9] Velazquez, E. A., Pujari, A., Boussalis, H. H., and Rad, K., "Frequency-Domain System Identification of a Large Segmented Space Reflector," *2005 IEEE International Symposium on Intelligent Control*, Vol. 1, Inst. of Electrical and Electronics Engineers, Piscataway, NJ, 2005, pp. 497–500.

[10] Lou, J. Z., Redding, D., Sigrist, N., Zhang, Y., and Basinger, S., "JWST On-Orbit Multi-Field Wave-Front Control with a Kalman Filter," *Optical Modeling and Performance Predictions II*, edited by M. A. Kahan, Proceedings of SPIE—The International Society for Optical Engineering, Vol. 5867, Society of Photo-Optical Instrumentation Engineers (International Society for Optical Engineering), Bellingham, WA, 2005, pp. 58670T-1–58670T-14.

[11] Fitzmaurice, M. W., Ha, K. Q., Le, C., and Howard, J. M., "End-to-End Performance Modeling of the James Webb Space Telescope (JWST) Observatory," *Optical Modeling and Performance Predictions II*, Proceedings of SPIE—The International Society for Optical Engineering, Vol. 5867, edited by M. A. Kahan, Society of Photo-Optical Instrumentation Engineers (International Society for Optical Engineering), Bellingham, WA, 2005, pp. 58670W-1–58670W-14.

[12] Hardaway, L. M. R., and Peterson, L. D., "Nanometer Scale Spontaneous Vibrations in a Deployable Truss Under Mechanical Loading," *AIAA Journal*, Vol. 40, No. 10, Oct. 2002, pp. 2070–2076.

[13] Briggs, H. C., and Needels, L., "Integrated Multidisciplinary Analysis of Segmented Reflector Telescopes," *Controls for Optical Systems*, edited by J. A. Breakwell, Proceedings of SPIE—The International Society for Optical Engineering, Vol. 1696, Society of Photo-Optical Instrumentation Engineers (International Society for Optical Engineering), Bellingham, WA, 1992, pp. 231–242.

[14] Melody, J. M., and Neat, G. W., "Integrated Modeling Methodology Validation Using the Micro-Precision Interferometer Testbed," *IEEE Conference on Decision and Control*, Vol. 4, Inst. of Electrical and Electronics Engineers, Piscataway, NJ, 1996, pp. 4222–4227.

[15] Chung, S. J., "Design, Implementation and Control of a Sparse Aperture Imaging Satellite," M.S. Thesis, Department of Aeronautics and Astronautics, Massachusetts Inst. of Technology, Cambridge, MA, 2002.

[16] Chung, S. J., Miller, D. W., and de Weck, O. L., "ARGOS Testbed: Study of Multidisciplinary Challenges of Future Space-Borne Interferometric Arrays," *Optical Engineering*, Vol. 43, No. 9, Sept. 2004, pp. 2156–2167. doi:10.1117/1.1779232

[17] Bell, K. D., Powers, M. K., Griffin, S. F., and Huybrechts, S. M., "Air Force Research Laboratory's Technology Programs Addressing Deployable Space Optical Systems," *Space Telescopes and Instruments V*, edited by P. Y. Bely and J. B. Breckinridge, Proceedings of SPIE—The International Society for Optical Engineering, Vol. 3356, Society of Photo-Optical Instrumentation Engineers (International Society for Optical Engineering), Bellingham, WA, 1998, pp. 535–551.

[18] Robertson, L., Griffin, S. F., Powers, M. K., Cobb, R., "Current Status of the UltraLITE Control Technology Testbed for Optical Mirror Mass Control," *Novel Optical Systems and Large Aperture Imaging Systems*, edited by K. D. Bell, M. K. Powers, and J. M. Sasian, Proceedings of SPIE—The International Society for Optical Engineering, Vol. 3430, Society of Photo-Optical Instrumentation Engineers (International Society for Optical Engineering), Bellingham, WA, 1998, pp. 209–218.

[19] Griffin, S. F., Robertson, L., Huybrechts, S. M., "Ultra-Lightweight Structures for Deployable Optics," *Novel Optical Systems and Large Aperture Imaging Systems*, edited by K. D. Bell, M. K. Powers, and J. M. Sasian, Proceedings of SPIE—The International Society for Optical Engineering, Vol. 3430, Society of Photo-Optical Instrumentation Engineers (International Society for Optical Engineering), Bellingham, WA, 1998, pp. 219–226.

[20] Denoyer, K., Erwin, R., and Ninneman, R., "Advanced Smart Structures Flight Experiments for Precision Spacecraft," *Acta Astronautica*, Vol. 47, No. 2–9, 2000, pp. 389–397. doi:10.1016/S0094-5765(00)00080-1

[21] Babuška, V., Erwin, R., and Sullivan, L., "System Identification of the SUITE Isolation Platform: Comparison of Ground and Flight Experiments," *AIAA Structures, Structural Dynamics, and Materials*

Conference—Smart Damping and Isolation, Vol. 3, AIAA, Reston, VA, 2003, pp. 2185–2195.
[22] Lake, M. S., Peterson, L. D., and Levine, M. B., "Rationale for Defining Structural Requirements for Large Space Telescopes," *Journal of Spacecraft and Rockets*, Vol. 39, No. 5, 2002, pp. 674–681.
[23] Hecht, E., *Optics*, 4th ed., Pearson Education/Addison Wesley, San Francisco, 2002, pp. 149–150, 393–397, 434, 467–469.
[24] Daniels, M., "Active Control of a Composite Optical Support Structure," M.S. Thesis, Univ. of New Mexico, Albuquerque, NM, 2004.
[25] PAM-VA One, Software Package, Ver. 1.1, ESI Group, Paris, 2005.
[26] Dyna-Mod, Software Package, Ver. 3.1, Mide Technology Corp., Medford, MA, 2005.
[27] Liu, K., Jacques, R., and Miller, D., "Frequency Domain Structural System Identification by Observability Range Space Extraction," *Journal of Dynamic Systems, Measurement, and Control*, Vol. 118, No. 2, June 1996, pp. 211–220.
[28] Schroeder, M., "Synthesis of Low Peak Factor Signals and Binary Sequences with Low Autocorrelation," *IEEE Transactions on Information Theory*, Vol. 16, No. 1, 1970, pp. 85–89. doi:10.1109/TIT.1970.1054411
[29] Lane, S., Lacy, S., Babuska, V., and Carter, D., "Correlation and Error Metrics for Plant Identification of On-Orbit Space Structures," *Journal of Spacecraft and Rockets*, Vol. 44, No. 3, May–June 2007, pp. 710–721. doi:10.2514/1.24583
[30] Lacy, S., and Babuska, V., "Input-Output Data Scaling for System Identification," *Proceedings of the International Federation of Automatic Control Symposium on System Identification* [CD-ROM], Elsevier, Oxford, 2006.
[31] Dorato, P., Abdallah, C., and Cerone, V., *Linear Quadratic Control, An Introduction*, Prentice Hall, Englewood Cliffs, NJ, 1995.
[32] Hoagg, J., Lacy, S., and Bernstein, D., "Broadband Adaptive Disturbance Rejection for a Deployable Optical Telescope Testbed," *Proceedings of the 2005 American Control Conference*, Vol. 7, Inst. of Electrical and Electronics Engineers, Piscataway, NJ, 2005, pp. 4953–4958.
[33] Quick Fringe, Software Package, Ver. 4.5, Diffraction Limited, Ottawa, Ontario, Canada, 2005.
[34] Mathcad, Software Package, Ver. 12, Parametric Technology Corp., Needham, MA, 2004.
[35] ZEMAX, Software Package, Ver. 10, ZEMAX Development Corp., Bellevue, WA, 2005.
[36] MATLAB, Software Package, Ver. 7, The MathWorks, Inc., Natick, MA, 2004.
[37] Lacy, S., Babuska, V., Schrader, K., and Fuentes, R., "System Identification of Space Structure," *Proceedings of the 2005 American Controls Conference*, Vol. 4, Inst. of Electrical and Electronics Engineers, Piscataway, NJ, 2005, pp. 2335–2340.
[38] Smith, W. J., *Modern Optical Engineering*, 3rd ed., McGraw–Hill, New York, 2000, pp. 356–357.

L. Peterson
Associate Editor